Non-basaltic asteroidal magmatism during the earliest stages of solar system evolution: A view from Antarctic achondrites Graves Nunatak 06128 and 06129

C.K. Shearer [a,*], P.V. Burger [a], C. Neal [b], Z. Sharp [c], L. Spivak-Birndorf [d], L. Borg [e], V.A. Fernandes [f,g], J.J. Papike [a], J. Karner [a], M. Wadhwa [d], A. Gaffney [e], J. Shafer [b], J. Geissman [c], N.-V. Atudorei [c], C. Herd [h], B.P. Weiss [i], P.L. King [a], S.A. Crowther [j], J.D. Gilmour [j]

[a] Institute of Meteoritics, Dept. of Earth and Planetary Sciences, Univ. of New Mexico, Albuquerque, NM 87131, USA
[b] Dept. of Civil Eng. and Geo. Sci., Univ. of Notre Dame, IN 46556, USA
[c] Dept. of Earth and Planetary Sciences, Univ. of New Mexico, Albuquerque, NM 87131, USA
[d] School of Earth and Space Exploration, Arizona State University, Tempe AZ 85287, USA
[e] Institute of Geophys. and Planetary Phys., Lawrence Livermore National Laboratory, Livermore, CA 94550, USA
[f] Berkeley Geochronology Center, 2455 Ridge Road Berkeley, CA 94709, USA
[g] Dept. Earth and Planetary Sciences, Univ. California – Berkeley, Berkeley, CA 94720, USA
[h] Dept. Earth & Atmospheric Sciences, University of Alberta, Edmonton, Alberta, Canada T6G 2E1
[i] Dept. of Earth, Atmos., and Planetary Sciences, Massachusetts Institute of Technology, Cambridge, MA 02139, USA
[j] School of Earth, Atmospheric and Environmental Sciences, University of Manchester, Oxford Road, Manchester M13 9PL, UK

Abstract

The recently recovered paired Antarctic achondrites Graves Nunatak 06128 and 06129 (GRA) are meteorites that represent unique high-temperature asteroidal processes that are identified in only a few other meteorites. The GRA meteorites contain high abundances of sodic plagioclase, relatively Fe-rich pyroxenes and olivine, abundant phosphates, and low temperature alteration. They represent products of very early planetesimal melting (4565.9 ± 0.3 Ma) of an unsampled geochemical reservoir from an asteroid that has characteristics similar to the brachinite parent body. The magmatism represented by these meteorites is contrary to the commonly held belief that the earliest stages of melting on all planetary bodies during the first 2–30 Ma of solar system history were fundamentally basaltic in nature. These sodic plagioclase-rich rocks represent a series of early asteroidal high-temperature processes: (stage 1) melting and partial extraction of a low-temperature Fe–Ni–S melt, (stage 2) small degrees of disequilibrium partial melting of a sodium- or alkali-rich chondritic parent body with additional incorporation of Fe–Ni–S melt that was not fully extracted during stage 1, (stage 3) volatile-enhanced rapid extraction and emplacement of the Na-rich, high-normative plagioclase melt, (stage 4) final emplacement and accumulation of plagioclase and phosphates, (stage 5) subsolidus reequilibration of lithology between 962 and 600 °C at an $f\mathrm{O_2}$ of IW to IW + 1.1, and (stage 6) replacement of merrillite and pyroxene by Cl-apatite resulting from the interaction between magmatic minerals and a Cl-rich fluid/residuum melt. The subsolidus events started as early as 4561.1 Ma and may have continued for upwards of 144 million years.

The existence of assemblages similar to GRA on several other planetary bodies with different geochemical characteristics (ureilite, winonaites, IAB irons) implies that this type of early asteroidal melting was not rare. Whereas, eucrites and angrites represent extensive melting of a parent body with low concentrations of moderately-volatile elements, GRA represents

---

* Corresponding author. Tel.: +1 505 277 9159.
  E-mail address: cshearer@unm.edu (C.K. Shearer).

low-degrees of melting of a parent body with chondritic abundances of moderately volatile elements. The interpretation of the low-temperature mineral assemblage is somewhat ambiguous. Textural features suggest multiple episodes of alteration. The earliest stage follows the interaction of magmatic assemblages with a Cl-rich fluid. The last episode of alteration appears to cross-cut the fusion crust and earlier stages of alteration. Stable isotopic measurements of the alteration can be interpreted as indicating that an extraterrestrial volatile component was preserved in GRA.

1. INTRODUCTION

Achondritic meteorites commonly represent remnants of magmatic systems from a diversity of planetary environments from differentiated planets (e.g., Moon, Mars) to asteroids (e.g., parent bodies of the HEDs, acapulcoites, lodranites) (Mittlefehldt et al., 1998 and references within). Many are products of the earliest stages of solar system magmatism and represent remnants of either whole planet melting such as the lunar ferroan anorthosites to low-degrees of melting such as the acapulcoites, lodranites, or brachinites. Many of these earliest stages of solar system magmatism were essentially basaltic in composition and started as early as 2 million years after CAI formation (Wadhwa et al., 1998, 2006). Much younger achondrites, such as lunar (3.8–2.8 Ga) and martian meteorites (4.5 Ga–150 Ma), represent episodes of mantle melting and secondary crust formation (Shearer et al., 2006; Wadhwa et al., 2006; Wadhwa, 2008). Newly discovered paired achondritic meteorites Graves Nunataks 06128 and 06129 (GRA) do not appear to fit within the planetary or petrologic context of any of these other achondrites. In contrast to the achondrites that suggest that all early solar system magmatism was predominantly basaltic in character, these two meteorites have a high content of sodic plagioclase and fairly Fe-rich silicates implying an "evolved" planetary igneous lithology. Initial studies of GRA suggest that this is not the case (Ash et al., 2008; Day et al., 2009; Shearer et al., 2008; Treiman et al., 2008; Zeigler et al., 2008).

The sodic plagioclase-rich lithologies as represented by GRA 06128 and 06129 are rare in meteorites and models for their origin fit within the context of only a few previous observations (Benedix et al., 1998; Ikeda and Prinz, 2001; Takeda et al., 2001). Minute, rare clasts and fragments containing sodic feldspar have been identified in chondrites and ureilites such as Kaidun, Adzhi-Bogdo, and Dar al Gani 319 (Ikeda and Prinz, 2001). Also, sodic plagioclase assemblages have been identified in winonaites (Benedix et al., 1998) and silicate inclusions in IAB iron meteorites (Takeda et al., 2001). Many of these studies suggested that these lithologies were produced by relatively low-degrees of partial melting of a chondritic precursor followed by inhomogeneous segregation, rapid extraction, and brecciation (Benedix et al., 1998; Ikeda and Prinz, 2001; Takeda et al., 2001).

Our initial study of GRA proposed that these two meteorites represent small degrees of partial melting of a chondrite source that had geochemical fingerprints similar to the brachinite parent body (Shearer et al., 2008). However, we were unable to define the specifics of such a melting process, its connection to other episodes of early asteroidal melting, the nature of subsolidus processes that are recorded in GRA, and the chronology of all of these events. Here, we summarize the findings of our consortium that has applied a wide range of analytical techniques to gain a fuller petrologic understanding of these unusual paired meteorites.

2. ANALYTICAL METHODS

Two thin section of these paired meteorites were studied (GRA 06129,23 and GRA 06128,55) along with a sample mass of approximately 6 g. The bulk sample was initially photo-documented prior to splitting the sample and forwarding these splits to members of the consortium. Two thin sections were initially documented using back-scattered electron (BSE) imaging with a JEOL 8200 electron microprobe at the University of New Mexico (UNM). False colored maps were created from these BSE images, which aided in the identification of major phases, namely plagioclase, olivine, orthopyroxene and clinopyroxene, as well as less abundant phases such as phosphates (apatite and merrillite), chromite, pentlandite, troilite and Fe, Ni metal. The false color map of GRA 06129,23 was used to determine the modal abundance of these phases. This map was point counted on a computer screen using a 2500 point grid. This produced a relative error of better than 3% for phases making up greater than 10% of the sample and better than 10% for phases making up between 1 and 9% of the sample (El-Hinnawi, 1966). Following phase identification, quantitative point analyses were conducted on the phases of interest, using an accelerating voltage of 15 kV, a beam current of 20 nA and a ~1 μm spot size. Phosphate analyses were conducted using a defocused, 10 μm spot in order to minimize beam volatilization. Ferric Fe was calculated using the equation of Droop (1987). Stoichiometric constraints used to determine the quality of the datasets, and detection limits were calculated at the 3σ level. Select phases (olivine, plagioclase, phosphates) were analyzed for a suite of trace elements using a Cameca 4f ims ion microprobe at UNM. The analytical approach used in this study followed the techniques described in Shearer and Papike (2005).

Major and trace element contents of a split of GRA 06129 were determined in duplicate. Approximately 1 g of GRA was powdered in a clean agate pestle and mortar. Two ~0.25 g aliquots were fused using a $LiBO_3$ flux and analyzed using inductively coupled plasma atomic emission spectroscopy (ICP-AES, University of Notre Dame) using the method described by Shafer et al. (2004). Two ~50 mg aliquots were dissolved using HF/HNO_3 digestions and analyzed for trace elements using an ELEMENT 2 high resolution magnetic sector inductively coupled plasma mass spectrometry (ICP-MS, University of Notre Dame) following the procedure described by Neal (2001). The reference

material BIR-1 was analyzed with both the major element and trace element analyses.

Micro-Fourier Transform Infrared (micro-FTIR) near-IR spectra (University of New Mexico) of the alteration areas cross-cutting the fusion crust in thin section were collected over a 50 μm by 100 μm area using a Nicolet Nexus 670 FTIR spectrometer with a Continμum microscope attachment. In addition, unpolarized near-IR and mid-IR spectra were collected on 100 μm by 100 μm areas of fine-grained portions of powdered alteration material using a micro-compression diamond cell. We targeted clumps of the powder where the grains appeared to be randomly oriented and small ($<\sim2$ μm). Each near-IR spectrum was collected over 10, 000–2100 cm^{-1} for 100–300 scans with 4 cm^{-1} resolution using a white-light source, CaF_2 beamsplitter, and MCT/A or MCT/A[*] detectors. Each mid-IR spectrum was collected over 5200–650 cm^{-1} for 100 scans with 4 cm^{-1} resolution using a Globar source, XT-KBr beamsplitter, and an MCT/A[*] detector. For all analyses, the samples were purged with dry air prior to and during spectra collection. A background spectrum was collected on an area of the thin section containing epoxy before each thin section analysis or on a clean area of diamond before each powder analysis.

Hydrogen, carbon, sulfur, and oxygen isotope analyses were made on bulk rock material at the University of New Mexico. Hydrogen, sulfur, and carbon measurements were made on untreated bulk samples. Oxygen measurements were made on a two different sample splits. One sample split that was untreated prior to analysis and a second sample split that was first cleaned with 1 M HCl.

Hydrogen was analyzed using a continuous flow system (Sharp et al., 2001) modified to allow for step heating. Samples were placed in a 6 mm quartz tube in a He stream. The quartz tube was heated with an external resistance heater. For each heating step, the evolved gas passed over a CuO trap heated to 650 °C to convert any H_2 to H_2O. The evolved water was then collected on a liquid nitrogen trap. At the end of a heating cycle, the liquid nitrogen was removed and the sample passed through a 1302 °C alumina tube lined with glassy carbon (Finnigan MAT TC-EA) for quantitative conversion of H_2O to H_2 and CO. The δD values of the H_2 gas were measured in a Finnigan MAT Delta[XL] Plus mass spectrometer in continuous flow using a calibrated H_2 gas a reference. All data are reported relative to VSMOW.

Carbon was analyzed in a similar manner. Samples were heated in a He–O_2 stream, passed through a heated CuO trap and evolved CO_2 was collected on a cold trap cooled with liquid nitrogen. Gas was analyzed in the same mass spectrometer in continuous flow. All data are reported relative to PDB.

For oxygen isotope measurements, one to two mg samples were fluorinated using BrF_5 as an oxidant, following the procedure described in Sharp (1995). O_2 gas generated from laser fluorination was cleaned by passage over a heated NaCl trap to remove any excess F_2 gas produced by breakdown of the BrF_5. The O_2 was adsorbed on two successive cold traps filled with 14× mol sieve to remove any traces of NF_3. Gore Mountain garnet (Valley et al., 1995) and San Carlos olivine (Kusakabe et al., 2004) were used as standards, both plotting on the terrestrial fractionation line.

Bulk sulfur abundance and the sulfur isotope composition were measured in a Finnigan MAT Delta[XL] Plus mass spectrometer in continuous flow using a calibrated S gas a reference. This method followed the approach used by Giesemann et al. (1994). All data are reported relative to CDT.

For radioisotopic dating by the $^{40}Ar/^{39}Ar$ method, step heating measurements were carried out at the Berkeley Geochronology Center. Prior to analyses, 25.52 mg of GRA 06129 were irradiated for 100 h in a Cd-shielded (to minimize undesirable isotopic interference reactions) CLIC-IT facility of the TRIGA reactor at Oregon State University, USA. Samples and the neutron fluence monitor PP-20 hornblende (the same as Hb3gr) were loaded into pits within aluminium disks. The J-values were calculated relative to an age of $Hb_3Gr = 1073.6 \pm 5.3$ Ma (Jourdan et al., 2006) and using the decay constants of Steiger and Jäger (1977). The correction factors for interfering isotopes correspond to the weighted mean of 10 years of measurements of K–Fe and $CaSi_2$ glasses and CaF_2 in the TRIGA reactor: $(^{39}Ar/^{37}Ar)_{Ca} = (6.95 \pm 0.09) \times 10^{-4}$, $(^{36}Ar/^{37}Ar)_{Ca} = (2.65 \pm 0.02) \times 10^{-4}$ and $(^{40}Ar/^{39}Ar)_K = (7.30 \pm 0.90) \times 10^{-4}$. Three bulk aliquots, weighing between 1.85, 2.30, and 2.95 mg, were degassed using a CO_2 laser with focused or a beam-integrator lens, and 21–69 heating steps were obtained. The gas was purified in a stainless steel extraction line using two C-50 getters and a cryogenic condensation trap. Argon isotopes were measured in static mode using a MAP 215-50 mass spectrometer with a Balzers electron multiplier, mostly using 10 cycles of peak-hopping. A detailed description of the mass spectrometer and extraction line is given by Renne et al. (1998). Blank measurements were obtained after every three sample runs. Mass discrimination was monitored several times a day and provided a mean value of 1.00731 ± 0.001318 per atomic mass unit. Ar isotopic data are corrected for blank, mass discrimination, interference, and radioactive decay.

Three samples (identified by their masses in micrograms: 330, 231, and 182) were analysed for xenon isotopes using the RELAX (Refrigerator Enhanced Laser Analyser for Xenon) mass spectrometer at the University of Manchester (Gilmour et al., 1994; Crowther et al., 2008). Samples were step-heated with a continuous wave Nd:YAG laser ($\lambda = 1064$ nm), for 1 min at a series of sequentially increasing laser powers. The gas extracted in each heating step was gettered (SAES, sintered Zr, ~350 °C) for 1 min to remove active gases before being admitted into the mass spectrometer. Data were acquired in 10-s segments, over a period of 5 min (30 consecutive segments). Isotope ratios and the signal intensity of a normalizing isotope calculated from the individual segments were extrapolated to determine the corresponding values at the time of gas inlet. A correction for discrimination was made with reference to interspersed air calibrations, which also allowed absolute gas quantities to be calculated. The procedural blank, ~1000 atoms ^{132}Xe, made a negligible contribution to the major releases on which our interpretation is based, so data presented here are not blank corrected.

Samples used for ^{26}Al–^{26}Mg analysis were initially processed in a clean laboratory at Lawrence Livermore National Laboratory. Several interior fragments from GRA 06129

weighing a total of ~185 mg were lightly crushed and leached for ~1 h in 1 N HCl at room temperature. The sample was then rinsed in ultrapure water and dried on a hotplate. All subsequent processing for the ^{26}Al–^{26}Mg isotopic analyses was conducted under clean laboratory conditions in the Isotope Cosmochemistry and Geochronology Laboratory (ICGL) in the School of Earth and Space Exploration at Arizona State University. A ~30 mg "whole rock" (WR) fraction from the leached bulk rock sample was digested using a 3:1 mixture of HF:HNO$_3$, followed by dissolution in concentrated nitric acid and finally in 1 N nitric acid. A ~5% aliquot was reserved for Al/Mg ratio measurements and ~3 to 4 mg equivalent aliquot was subjected to column chromatography for separating Mg for high precision Mg isotope ratio measurements. Two ~1 to 2 mg plagioclase mineral separates were handpicked from the remainder of the leached bulk sample and subsequently processed in the same way as the whole rock fraction. Column chromatographic procedures for Mg separation have been described in detail elsewhere (Teng et al., 2007; Spivak-Birndorf et al., 2009). Mg isotope ratio analyses were conducted with a Thermo Neptune multicollector inductively coupled plasma mass spectrometer (MC-ICPMS) in the ICGL using analytical protocols similar to those described by Spivak-Birndorf et al. (2009). Radiogenic excesses in ^{26}Mg from the decay of ^{26}Al (Δ^{26}Mg) were calculated by normalizing all measured ^{26}Mg/^{24}Mg ratios to a ^{25}Mg/^{24}Mg ratio of 0.12663 (Catanzaro et al., 1966) using the exponential law and comparing the normalized ^{26}Mg/^{24}Mg ratio in the sample to the mean of the normalized ^{26}Mg/^{24}Mg ratios of the bracketing standards.

Magnetic properties were measured at the University of New Mexico using a DC-SQUID based superconducting rock magnetometer (2G Enterprises), housed in a low magnetic induction space. The specimen mass used for all measurements was approximately 120 mg. First, the specimen was subjected to repeated measurements of the natural remanent magnetization (NRM) to test for viscous remanent magnetization (VRM) acquisition. Alternating field (AF) demagnetization was utilized to a peak field of 120 mT, to examine the character of the remanence carried by relatively low coercivity phases. An anhysteretic remanent magnetization (ARM) was acquired in a DC field of 0.1 mT and a peak AF of 98 mT. Acquisition of an isothermal remanent magnetization (IRM) to near saturation (SIRM) utilized a pulse DC impulse magnet to about 3.0 T. Backfield pulse DC demagnetization of near saturation IRM was conducted until IRM changed sign. AF demagnetization of IRM imparted in a pulse DC field of 98 mT was carried out to 100 mT. The specimen was subsequently mounted in pure alumina cement to make a thermally resistant specimen of cubic shape, and subjected to progressive thermal demagnetization to over 670 °C of three-component IRM, acquired in orthogonal fields of 3.0, 0.3, and 0.03 T, following the method of Lowrie (1990).

3. RESULTS

3.1. Modal mineralogy, textures, and distribution of phases

On a macroscopic scale, the two meteorites consist of gray crystalline material with a strong foliation and a weathering typified by a rusty to yellow-ocher colored alteration (Satterwhite and McBride, 2007). The foliation is defined by parallel fractures. Approximately 40–50% of the exterior has a pitted and fractured glassy black fusion crust (Satterwhite and McBride, 2007). Thin section GRA 06129,23 exhibits a heterogeneous, granoblastic texture (Fig. 1A) with a modal mineralogy dominated by fairly sodic plagioclase ($\approx$81%). Thin section GRA 06128,55 has similar overall textural characteristics but also illustrates the relationship between the fusion crust and both high- and low-temperature mineral assemblages (Fig. 1B). In both thin sections, masses of plagioclase are separated by lenses and blocky masses of ferromagnesian silicates, oxides, and sulfides. Two pyroxenes (orthopyroxene and Ca-rich clinopyroxene) and olivine are the most common silicates after plagioclase, making up approximately 9% and 8%, respectively. Large olivine grains contain composite inclusions of Fe–Ni metal, troilite, and pentlandite (Fig. 2A). The ferromagnesian mineral enriched masses exhibit both a poikilitic and a granulitic texture. In the former, olivine and sulfide are surrounded by a thin armor of high-Ca pyroxene (Fig. 2B). The high-Ca pyroxene exhibits exsolution of low-Ca pyroxene on the scale of 2 μm or less (Fig. 2C). Apatite overgrowths on merrillite occur in masses of up to 600 μm (Fig. 2D). Merrillite also occurs as small partially absorbed inclusions in apatite. Merrillite occurs along the grain boundary between apatite and either olivine or low-Ca pyroxene. Although these are the textural relations that Treiman et al. (2008) may have interpreted as indicating the merrillite was replacing Cl-rich apatite, our interpretation is that this merrillite was protected from alteration to apatite at these grain boundaries. In several areas, it appears that phosphates are replacing augite or are intergrown with low-Ca pyroxene (Fig. 2B). The modal abundance of phosphates is approximately 0.5%, although higher modal abundances have been documented (Treiman et al., 2008; Zeigler et al., 2008). Trace abundances of ilmenite and chromite are distributed throughout the section both within and outside of the mafic masses. The metal and sulfide (troilite and pentlandite) inclusions in the olivine have an intimate textural relationship suggesting a common petrogenesis. The pentlandite occurs as discrete blebs (Fig. 3) or lamellae within troilite. Fe–Ni metal appears to be spatially associated with the pentlandite. In some cases, individual inclusions contain all three phases (Fig. 3).

A megascopic view of the GRA meteorites indicates they have undergone significant low-temperature alteration. The microscopic view indicates this alteration is pervasive along grain boundaries and in fractures within mineral grains. At least three types of low-temperature alteration exist in this meteorite: alteration that is fine-grained, dark, and iron-rich, alteration that is iron-rich with perhaps S- and Cl-bearing phases, and alteration of olivine to "iddingsite" (Fig. 4). Based on the two thin sections studied there appears to be some zoning in the distribution of these alteration assemblages and well defined cross-cutting relationships. The fusion crust viewed in thin section GRA 06128,55 is relatively unaltered. Alteration lines vesicles in the fusion crust. The Fe- and S-rich veining cuts
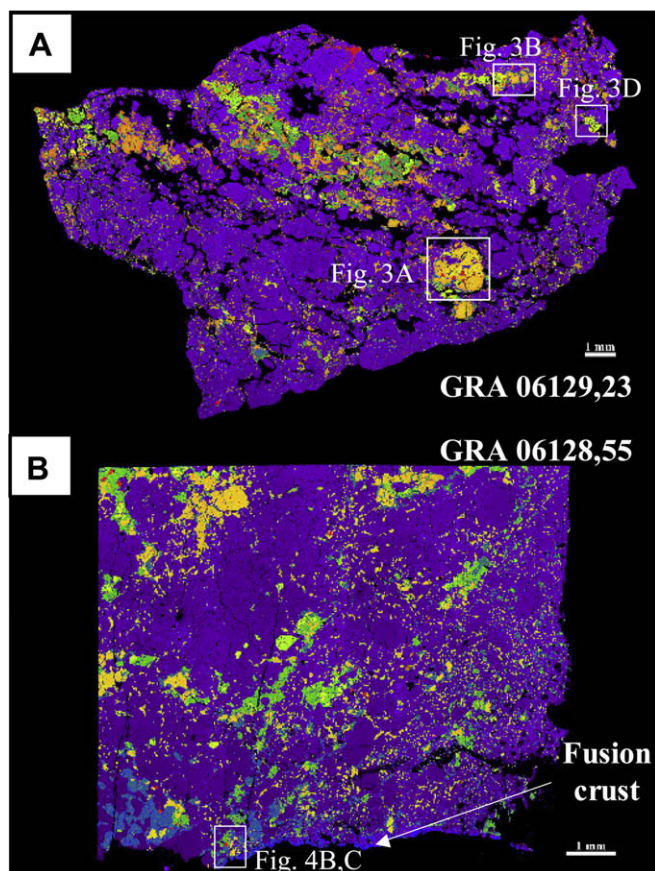
Fig. 1. Composite, false color backscatter electron (BSE) images of (A) thin section GRA 06129, 23 and (B) a portion of thin section GRA 06128,55 adjacent to the fusion crust (on the lower portion of the image). Color code: purple, plagioclase; blue, orthopyroxene and clinopyroxene; orange-yellow, olivine; blue-green, phosphates; red, Fe-bearing oxides, sulfides and metals. Selected fields enlarged in Fig. 2.

across the fusion crust and other episodes of alteration (Fig. 4). The relationship between the other two episodes of alteration is less clear and therefore it is uncertain to what degree this alteration is parent body vs terrestrial.

3.2. Mineral chemistry

Mineral chemistries and formulae for most high-temperature phases are summarized in Table 1. Plagioclase is fairly homogeneous and exhibits no systematic variations within individual grains or among different textural relations (coarse vs fine grain, within vs outside of masses dominated by mafic silicates). The plagioclase ranges in composition from $An_{17}Ab_{83}Or_2$ to $An_{13}Ab_{85}Or_2$ ($n = 143$), although 93% of the plagioclase has an even more restricted composition of An_{14-15}. Plagioclase is light REE enriched ($La_{CI\ normalized}/Yb_{CI\ normalized} > 10$) with a positive Eu anomaly ($Eu_{CI\ normalized}/Sm_{CI\ normalized} \sim 100$) (Fig. 5). Barium and Sr exhibit limited variation in the plagioclase with average ($n = 10$) concentrations of 77.0 ppm and 94.5 ppm, respectively.

The composition of olivine is also fairly restricted (Fig. 6) with regards to Mg# (Fo_{41-40}) and Cr_2O_3 (0.00–0.07 wt.%), but CaO (0.01–0.17 wt.%) is variable. One olivine grain adjacent to a chromite has a slightly higher Mg#

(Fo_{45-42}) and Cr_2O_3 (0.02–0.31 wt.%). This is attributed to reequilibration between the chromite and olivine at subsolidus temperatures. Based on the stoichiometry of approximately 50 microprobe analyses, the iron in olivine is essentially all ferrous. Nickel in the olivine ranges from 1177 to 1584 ppm, whereas Co exhibits a somewhat more limited range from 500 to 592 ppm (Fig. 7). The concentrations of Ni and Co in olivine are not a result of small Fe–Ni metal inclusions as these inclusions are more closely associated with very visible sulfide inclusions that could be avoided during analysis. The Ni and Co contents in the olivine from GRA are substantially higher than those observed in olivine from other asteroid magmatic systems represented by the HEDs and the unique achondrite QUE 93148 (Shearer et al., 2008). Vanadium and Ti in the olivine are 8–10 ppm and 75–95 ppm, respectively.

The high-Ca pyroxene ranges in composition from En_{39}-$Fs_{16}Wo_{45}$ to $En_{44}Fs_{29}Wo_{27}$ (Fig. 6). Beam overlap between pyroxene host and exsolution lamellae during electron microprobe analysis results in the extension of the pyroxene compositions to lower Wo on the pyroxene quadrilateral (Fig. 6). The compositional variation in orthopyroxene is limited with an average composition of $En_{53}Fs_{45}Wo_2$ (Fig. 6). There is approximately 2–3% "others" components (Na, Fe^{3+}, Al^{VI}, Ti, Mn) in the M1–M2 site of the high-Ca
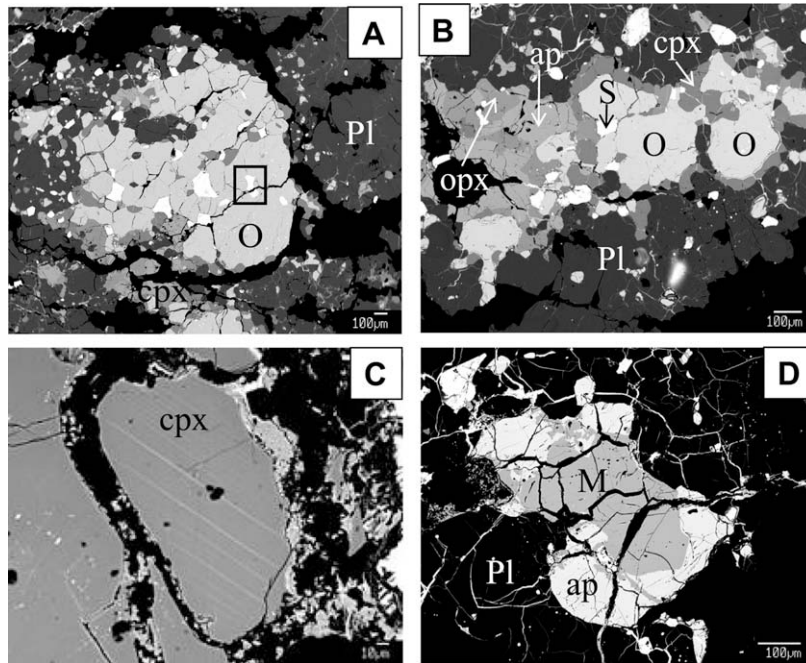
Fig. 2. BSE images of phases in GRA 06129,23. (A) Image of subhedral olivine grain (O) with inclusions of sulfides and metal. Highlighted area is magnified in Fig. 3. (B) Image illustrating the poikilitic texture among silicates, sulfides, and phosphates with clinopyroxene enclosing olivine and troilite (S) and apatite (ap)-orthopyroxene intergrowths. (C) Low-Ca pyroxene exsolution in high-Ca pyroxene host. (D) Phosphate intergrowth with apatite (ap) enclosing merrillite (M). Other phases in this figure are designated as Pl, plagioclase; cpx, high-Ca pyroxene; opx, low-Ca pyroxene.
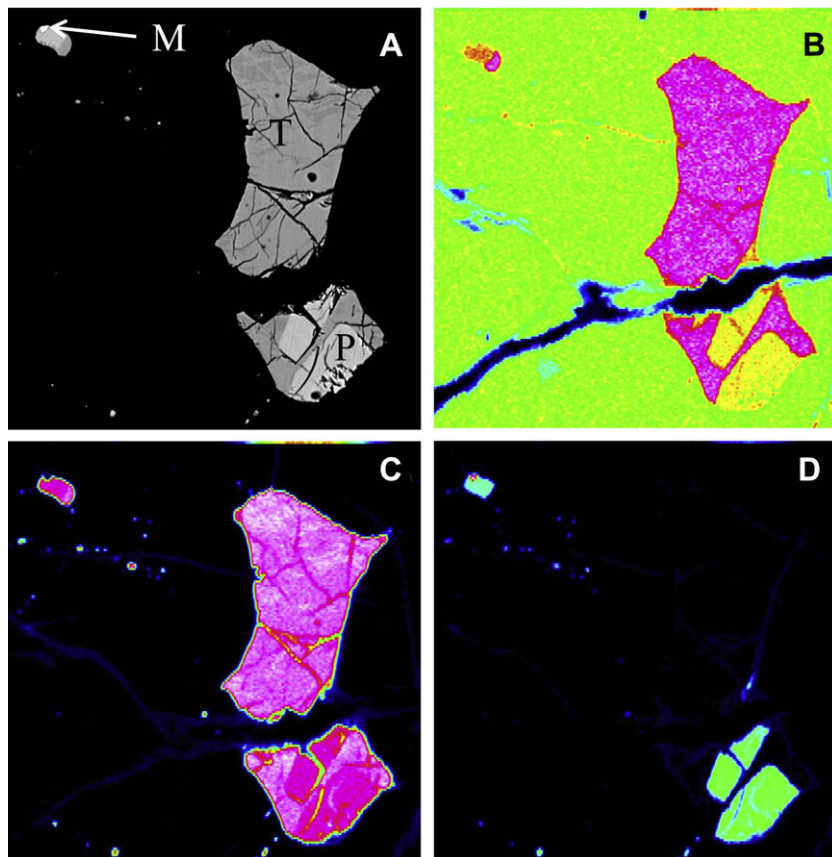
Fig. 3. (A) BSE image of sulfide–metal inclusions in olivine from Fig. 2A. The large sulfide grain illustrates the textural relationship between pentlandite and troilite. The tiny grain in the upper left hand corner illustrates Fe–Ni metal (M) adjacent to pentlandite (P) which is adjacent to troilite (T). X-ray maps further illustrate the relationship among these phases. (B) Fe X-ray map. (C) S X-ray map. (D) Ni X-ray map.
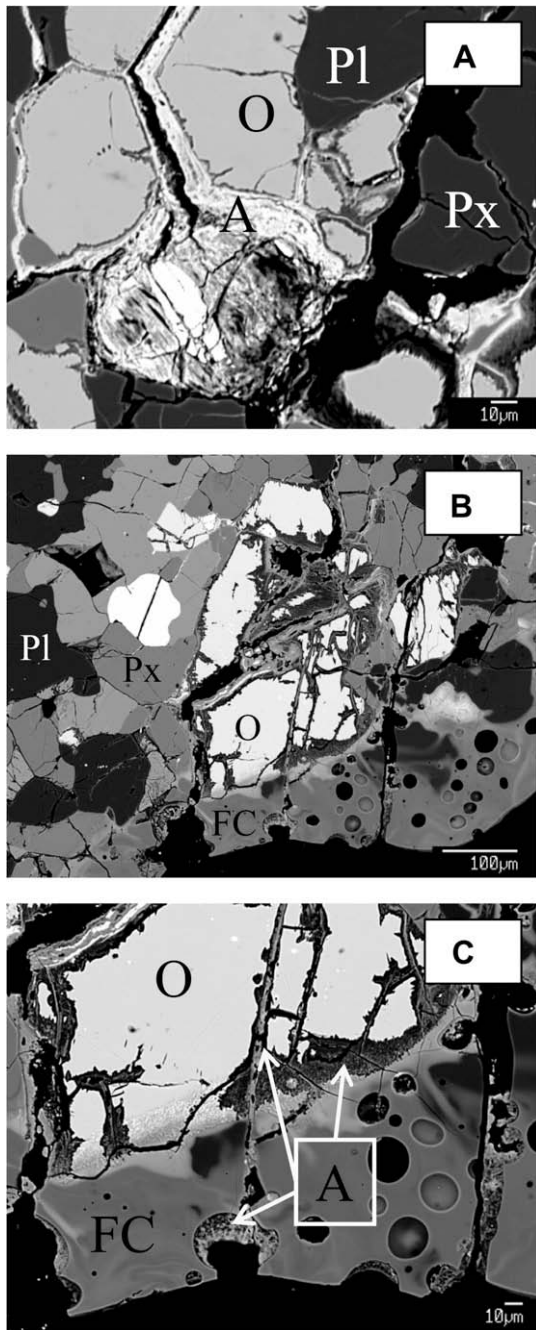
Fig. 4. BSE image low T alteration associated with GRA. (A) GRA 06129,23 illustrating alteration cutting across olivine and adjacent to mineral boundaries. (B) GRA 06128,55 illustrating relationships between fusion crust and alteration. Image also illustrates multiple generations of alteration. (C) Enlarged image of fusion crust-alteration relationships in GRA 06128,55 that is depicted in Fig. 1B. FC, fusion crust; O, olivine; A, alteration; Pl, plagioclase; Px, pyroxene.

pyroxene, whereas these components makeup only 1% of the M1–M2 site in orthopyroxene. Based on the stoichiometry of approximately 100 microprobe analyses, the average ferric iron ($Fe^{3+}/(Fe^{3+} + Fe^{2+})$) in the high-Ca pyroxene is 7%. As expected, the orthopyroxene has less ferric iron (commonly less than 1% total iron).

Apatite is halogen-rich (Cl ≈ 5.6%, F ≈ 0.7%), whereas the merrillite is halogen-poor with substantial Na in the CaIIA site (≈2.5%) (Table 1). REE pattern of the apatite is slightly LREE enriched (≈10–15 × CI) relative to HREE (≈6–10 × CI) with a positive Eu anomaly (Fig. 5). The merrillite is at least 12.5 times more enriched in REE relative to apatite. The merrillite pattern is enriched in MREE relative to both LREE and HREE and has a negative Eu anomaly (Fig. 5).

A significant number of phases make up the oxide, metal, and sulfide assemblages. Based on stoichiometry, the microprobe analyses of ilmenite indicate that it does not contain a substantial hematite component. The ilmenite does contain approximately 7% of a geikielite ($MgTiO_3$) component. The chromite composition is dominated by a chromite with minor spinel and ulvöspinel components. Chromite stoichiometry suggests a range in ferric iron content from less than 0.5 wt% Fe_2O_3 adjacent to olivine to 3.25 wt% Fe_2O_3 along the rims of the chromite. Sulfide–metal assemblages exhibit distinct differences between those occurring as inclusions in olivine compared to those associated with surrounding feldspar or mafic assemblages. Pentlandite–troilite–metal assemblages in the olivine are characterized by high-Ni metal and low-Ni troilite, whereas the troilite–pentlandite assemblage in the surrounding matrix is more Ni enriched (Fig. 8).

The low-temperature alteration that occurs along fractures and on mineral surfaces is generally Fe-rich and very heterogeneous on the scale of a microprobe beam diameter of 1–3 μm. The Fe-enrichment is attributed to the high abundance of Fe phases making up the alteration mineral assemblage. Mössbauer spectra collected and reported by Treiman et al. (2008) indicate a range of ferric iron in the "nanophase" iron oxide in the alteration. The alteration mineralogy is relatively low in Al_2O_3 and exhibits substantial variation in SiO_2 and CaO (Fig. 9).

3.3. Geochemistry

3.3.1. Major elements

Some care should be taken in the interpretation of the bulk rock, major element composition of this meteorite as it contains both high-temperature and Fe-rich low-temperature components (Table 2). As expected from the mineralogy of GRA 06128 and GRA 06129, the bulk rock is high in Al_2O_3 (15.5 wt.%), CaO (6.22 wt.%), and Na_2O (7.51 wt.%). The CaO/Al_2O_3 is 0.40. Moderately-volatile elements such as Na and K are near chondritic proportions. For GRA the K/Na ratio is 0.04, whereas that ratio is approximately 0.11 for L and CI chondrites. The MnO/FeO is 0.0086 (assuming total Fe as FeO). The Mg# of the bulk rock does not reflect the magmatic and metamorphic history of this lithology due to the high Fe (and ferric iron) content of the alteration products. Better constraints on the Mg# of the bulk rock may be obtained from the Mg# of the pyroxene and olivine. These silicates indicate that the bulk rock has a fairly low Mg# (less than 40). The high phosphate modal abundance is evident in the overall P_2O_5 of the bulk rock (0.19%).

Table 1
Examples of major, minor, and trace element chemistry of mineral phases in GRA06129.

Olivine		Pyroxene			Plagioclase
		Opx	Opx	Cpx	
Analyses by mass					
SiO_2	33.93	52.21	52.49	52.65	64.71
Al_2O_3	0.00	0.20	0.44	0.42	23.31
TiO_2	0.02	0.21	0.42	0.33	N/A
Cr_2O_3	0.00	0.10	0.38	0.37	N/A
Fe_2O_3	N/A	0.27	0.65	0.91	N/A
MgO	18.28	18.65	13.72	13.09	0.02
FeO	48.62	27.30	13.60	10.51	0 40
MnO	0.73	0.61	0.36	0.29	N/A
CaO	0.11	1.08	18.29	21.68	2.99
Na_2O	0.00	0.02	0.28	0.29	9.83
K_2O	N/A	N/A	N/A	N/A	0.33
Total	101.68	100.64	100.62	100.54	101.59

Cations based on 4 oxygens		Cations based on 6 oxygens				Cations based on 8 oxygens	
Si	0.994	Si	1.985	1 974	1.973	Si	2.814
Al	0.000	^{IV}Al	0.009	0.019	0.019	^{IV}Al	1.195
Total (tetrahedral site)	*0.994*	*Total (tetrahedral site)*	*1.994*	*1.993*	*1.992*	*Total (tetrahedral site)*	*4.009*
Ti	0 001	Ti	0.006	0.012	0.009	Fe	0.015
Cr	0 000	^{VI}Al	0.000	0.000	0.000	Mg	0.001
Mg	0 798	Fe^{3+}	0.008	0.019	0.026	Ca	0.139
Ca	0 004	Cr	0.003	0.011	0.011	Na	0.829
Mn	0 018	Fe^{2+}	0.868	0.428	0.329	K	0.018
Fe^{2+}	1 191	Mn	0.019	0.012	0.009	Total cations	5.011
Na	0 000	Mg	1.057	0.769	0.731		
S	0 000	Ca	0.044	0.737	0.871		
Total (octahedral site)	2.012	Na	0.001	0.020	0.021		
		Total (M1 and M2)	2.006	2.007	2.008		

Trace element analyses (in ppm)		Molecular proportions of wollastonite (Wo), enstatite (En), and ferrosilite (Fs)				Molecular proportions of orthoclase (Or), albite (Ab), and anorthite (An)	
Sc	13.75	Wo	2.2	38.1	45.1	Or	1.9
Ti	76.28	Er	53.7	39.8	37.9	Ab	84.0
V	8.79	Fs	44.1	22.1	17.0	An	14.1
Cr	61.43						
Mn	11508.35						
Co	526.21					Trace element analyses (in ppm)	
Ni	1367.33					Ba	77.19
Y	0.16					Sr	94.77

	Oxides			Metal and sulfides			Phosphates	
	Chromite	llmenite		Troilite	Pentlandite	Fe.Ni Metal	Apatite	Merrillite
Analyses by mass								
TiO_2	11.65	54.35	Ti	0.00	0.00	0.00	P_2O_5	41.25	46.07
SiO_2	0.00	0.00	Cr	0.00	0.00	0.00	SiO_2	0.00	0.00
Al_2O_3	4.55	0.08	Fe	62,56	37.73	34 28	Ce_2O_3	0.00	0.02
Cr_2O_3	38.40	0.30	Ni	0.00	26.24	6088	Y_2O_3	0.00	0.00
Fe_2O_3	0.73	0.00	Co	0 12	2.53	1.11	MgO	0.05	2.68
v_2o_3	2.77	0.56	S	36.76	33.47	425	CaO	53.62	46.92
FeO	40.79	43.81	P	0.00	0.00	0.00	FeO	0.09	1.69
MgO	1.48	2.01	Total	99.45	99.96	100.52	Na_3O	0.41	2.59
MnO	0.53	0.62					F	0.41	0.00

(*continued on next page*)

Table 1 (continued)

	Oxides			Metal and sulfides				Phosphates	
	Chromite	Ilmenite		Troilite	Pentlandite	Fe.Ni Metal		Apatite	Merrillite
NiO	0.00	0.00					CI	5.62	0.00
Total	100.89	101.72					$F_3 = -O$	0.17	0.00
							$Cl_2 = -O$	1.27	0.00
							Total	100.00	99.98
*Cations			Cations				§Cations		
Ti	2.502	0.996	Ti	0.000	0.000	0.000	P	3.003	14.021
Si	0.000	0.000	Cr	0.000	0.000	0.000	Si	0.000	0.000
Al	1.531	0.002	Fe	0.494	0.306	0.341	Ce	0.000	0.003
Cr	8.673	0.006	Ni	0.000	0.202	0.576	Y	0.000	0.000
Fe^{3+}	0.157	0.000	Co	0.001	0.019	0.010	Mg	0.006	1.436
V	0.634	0.011	S	0.505	0.472	0.074	Ca	4.946	18.09
Fe^{2+}	9.746	0.893	P	0.000	0.000	0.000	Fe	0.006	0.509
Mg	0.629	0.073	Total cations	1.000	1.000	1.000	Na	0.069	1.807
Mr	0.128	0.013					F	0.111	
Ni	0.000	0.000					Cl	0.818	
Total cations	24.000	1.994					Total cations	8.030	35.870

*Based on 24 cations per 32 oxygens for chromite, and 2 cations per 3 oxygens for llmenite.
§Based on 24 cations per 32 oxygens for chromite, and 2 cations per 3 oxygens for ilmenite.

The normative mineralogy is dominated by plagioclase and diopside. Sulfide (in the form of pyrite) and apatite are important normative accessory minerals. Nepheline occurs in the normative mineralogy suggesting that this is silica undersaturated bulk rock composition. However, the occurrence of nepheline in the norm of this bulk rock is the result of including the iron in the low-temperature alteration.

3.3.2. Trace elements

Trace element characteristics of the bulk meteorite are presented in Table 2. Although the high Na content and abundant phosphates imply an "evolved rock", the overall trace element characteristics do not support this inference. The REE pattern is fairly flat (1 to 2 × CI chondrite) with a positive Eu anomaly (5 × CI chondrite) (Fig. 5). This suggests that primarily the phosphates and plagioclase dictate the REE pattern (Fig. 5). Elements more volatile than Na and K (i.e., Rb and Cs) appear to be depleted relative to chondrites. The K/Rb and K/Cs for GRA are higher than chondrite (i.e., K/Rb = 1300 vs 330 and K/Cs = 69,000 vs 3000 compared to L chondrites). The depletions of these
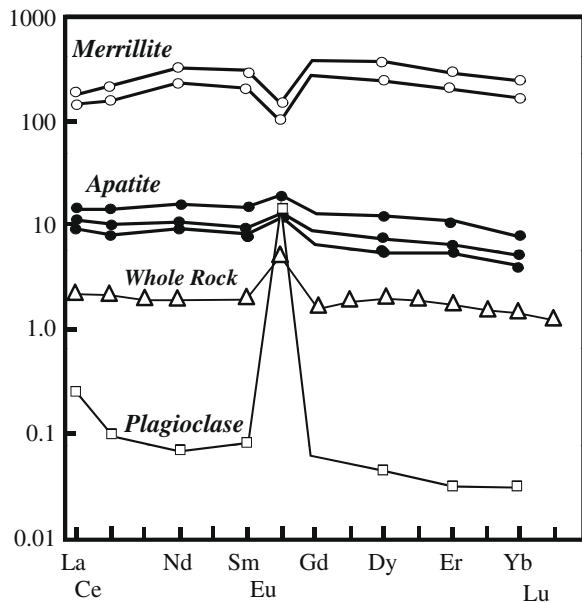

Fig. 5. Chondrite normalized REE patterns of GRA 06129 whole rock and selected minerals (plagioclase, apatite and merrillite). Whole rock data was determined by ICP-MS, whereas mineral data was determined by ion microprobe. Patterns normalized to CI chondrite values taken from Anders and Grevesse (1989).
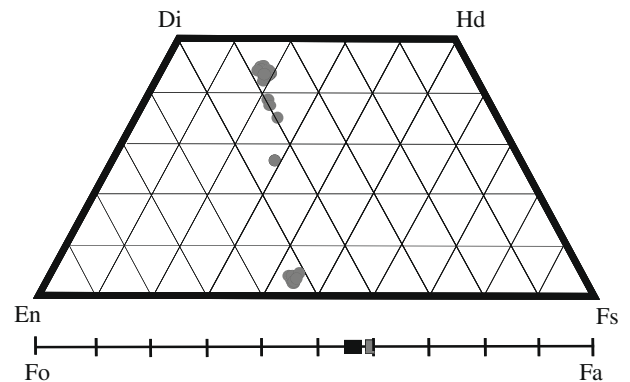

Fig. 6. Compositions of olivine and pyroxene in GRA 06129,23. Olivine composition represented by red field is a single olivine in direct contact with chromite.
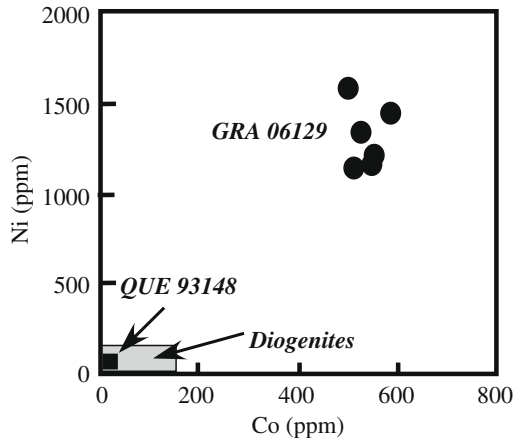
Fig. 7. Plot of Co vs Ni for olivine in GRA 06129,23. Included for comparison is the field for olivine in diogenites from the HED parent body (4 Vesta) and olivine in meteorite QUE 93148. QUE 93148 has been suggested to represent the mantle of the HED parent body or the pallasite parent body.

volatile elements are correlated with their volatilities (Na = K > Rb > Cs), whereas incompatible elements such as Zr, Y, and Nb are 1 to 3 × CI. Strontium, which occurs in the phosphates and plagioclase, is enriched relative to CI chondrites. The bulk Rb/Sr is 0.02. This value is substantially less than $(Rb/Sr)_{CI}$ (=0.295). Nickel and Co are 2215 ppm and 297 ppm, respectively. The bulk Ni/Co (=7.46) of GRA is substantially less than $(Ni/Co)_{CI}$ of 21.9.

The ratios $(Na/Sc)_{CI}$ and $(Sm/Sc)_{CI}$ are proxies for the role of plagioclase/pyroxene and melt/pyroxene, respectively, in the petrogenesis of primitive achondritic meteorites (Fig. 10). Whereas GRA 06129 has $(Na/Sc)_{CI}$ and $(Sm/Sc)_{CI}$ greater than 1, acapulcoites, lodranites, ureilites, winonaites, and brachinites generally have values that are near CI or sub-CI. Potential proxies of sulfide/silicate melt (Cu/Sm), sulfide/pyroxene (Cu/Sc), and sulfide/metal (Cu/Co) exhibit fractionation from CI. For GRA 06129, all of these ratios are sub-chondritic with $(Cu/Sm)_{CI} = 0.09$, $(Cu/Sc)_{CI} = 0.31$, and $(Cu/Co)_{CI} = 0.42$.

3.4. Stable isotopes

Stable isotope data are summarized in Table 3 and Fig. 11. The oxygen isotope composition was measured in duplicate, with a $\delta^{17}O$ and $\delta^{18}O$ value averaging 2.85‰ ($1\sigma = 0.04$) and 5.83‰ ($1\sigma = 0.13$). The $\Delta^{17}O$ value defined as $\Delta^{17}O = \delta^{17}O - 0.52\delta^{18}O$ (e.g., Sharp, 2007) is −0.18‰ ($1\sigma = 0.01$). Our $\Delta^{17}O$ value is identical to that reported by Zeigler et al. (2008). If a slope for the terrestrial fractionation line of 0.526 is used (Zeigler et al., 2008), the $\Delta^{17}O$ value is given by −0.217‰.

The vast majority of hydrogen is released between 200 °C and 350 °C. The corresponding δD values are between −121‰ and −153‰ (SMOW). Carbon release begins above 145 °C and is essentially complete below 467 °C (gas collected during ramping between 317 °C and 467 °C). The $\delta^{13}C$ values of all samples are similar, averaging −25.5‰ (relative to PDB).

The sulfur isotopes were also measured on a sample of the bulk meteorite. Therefore, the reported values are for a combination of the primary igneous assemblage and the alteration. The bulk meteorite has between 2.1 and 2.5 weight% sulfur. The unaltered portion of the meteorite has significant S as indicated by the high modal abundances of troilite and pentlandite. The alteration assemblage has a significant variation in S from less than 0.1 weight% to 20 weight%, with an average S content of 2.7 weight%. The $\delta^{34}S$ values for two splits of GRA 06129 are −1.05‰ and −0.55‰.

3.5. Ar and Xe isotope measurements

^{40}Ar–^{39}Ar step heating data for the three bulk fragments of GRA 06129 are reported in Table 4, and $^{40}Ar/^{36}Ar$ vs. $^{39}Ar/^{36}Ar$ in Fig. 12. A total of 69 heating steps, comprising ∼65% of the total ^{39}Ar release, were acquired for aliquot-1 giving a complex release namely for the low and intermediate temperature steps. Data derived from each heating step are presented in electronic annex EA-1. The apparent ages for these steps are in most part well above the age of the Solar System and thus have no chronologic meaning. Based on attempts to correct for either trapped and/or cosmogenic $^{40}Ar/^{36}Ar$, the complex release over the low temperature steps suggest more likely the redistribution of radiogenic argon rather than the contribution from the former components. For the last 10 heating steps, a plateau comprising ∼35% of the total ^{39}Ar release gives an age of 4.425 ± 0.016 Ga. This age is the same as that obtained for the slope of the correlation line in a $^{40}Ar/^{36}Ar$ vs $^{39}Ar/^{36}Ar$ plot, 4.424 ± 0.032 Ga, over these high temperature steps. The trapped $^{40}Ar/^{36}Ar$ component for these high temperature steps is negligible, thus no correction was performed. Argon age spectra for aliquots-2 and 3 suggest a partial degassing over the initial 8–11% of ^{39}Ar release and corresponding to an age of $\leqslant 2.673 \pm 0.038$ Ga. The reminder 89–92% of ^{39}Ar release give well defined plateaus corresponding to ages of 4.473 ± 0.016 Ga (aliquot-2) and 4.467 ± 0.018 Ga (aliquot-3), and having no contributing trapped $^{40}Ar/^{36}Ar$. These ages are indistinguishable from those obtained from the slope on the $^{40}Ar/^{36}Ar$ vs. $^{39}Ar/^{36}Ar$ isochron line, 4.460 ± 0.032 Ga (aliquot-2) and 4.463 ± 0.010 Ga (aliquot-3). Apparent age (Ga) vs cumulate ^{39}Ar release per step and $^{38}Ar/^{36}Ar$ vs fraction ^{39}Ar released for the three bulk aliquots are shown in electronic annex EA-2 and EA-3, respectively. In Fig. 12, it is shown the data for the three aliquots analysed in a $^{40}Ar/^{36}Ar$ vs. $^{39}Ar/^{36}Ar$ plot. The correlation line corresponds to a regression over all the data considered on the three plateaus. The slope of the correlation line on the $^{40}Ar/^{36}Ar$ vs. $^{39}Ar/^{36}Ar$ plot with all the data in the plateaus correspond to an age of 4.460 ± 0.028 Ga.

The overall pattern of the Ca/K spectra for the three GRA 06129 aliquots shows a constant value of ∼10 along the individual spectra. However, there is a slight increase (Ca/K = 13–16) at intermediate temperatures suggesting argon release from a phase(s) relatively enriched in Ca (e.g., apatite and/or pyroxene).

The $^{38}Ar/^{36}Ar$ values show complex patterns likely to involve one or more Cl-rich phase(s). In Table 4, ^{38}Ar (moles)
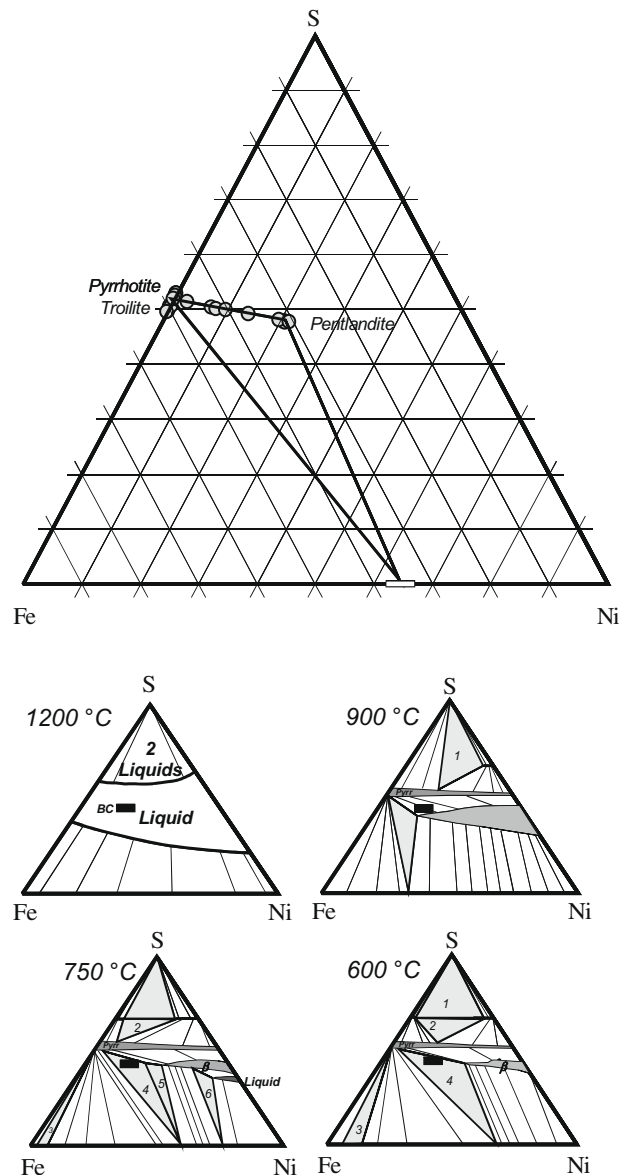
Fig. 8. GRA metal and sulfide compositions represented in the S–Fe–Ni system. Inserted in the diagram are experimentally and thermodynamically determined phase relationships in that system at 1200, 900, 750, and 600 °C (after Hsieh et al., 1987). The numbers (1–6) designate 3 phase fields in the isothermal sections. Approximate bulk composition (BC) of sulfide inclusions is inserted in the diagram and is based on modal abundance of metal and sulfide phases. The crystallization history of the sulfide–metal intergrowths can be reconstructed based on these isothermal sections. At 1200 °C, the estimated BC is a liquid. By 900 °C, the BC consists of a Fe sulfide and a Fe–Ni–S melt assemblage. The composition of each is defined by appropriate tie lines. At approximately 750 °C, BC is in field 4 which represents a mineral assemblage of coexisting of Fe–Ni metal–Fe sulfide–β Fe, Ni sulfide. Finally, BC is in field 4 in the 600 °C isothermal section which represents a mineral assemblage coexisting of Fe–Ni metal–Fe sulfide–β Fe, Ni sulfide. At this lower temperature, the Fe, Ni sulfide is more Ni-rich than the three phase assemblage 750 °C.

are reported for each aliquot and show that the three aliquots have different amounts of ^{38}Ar, with aliquot-3 having ~1.5 times more ^{38}Ar than aliquots 1 and 2. Aliquots 2 and 3 show ^{38}Ar/^{36}Ar values at intermediate temperatures well above the cosmogenic value (1.54), between 2.2 and 13.1. For these steps there is no evidence for terrestrial contamination, which is usually seen as a decrease in the Ca/K most notably at low-temperature heating steps. Instead, this is likely due to the existence of a Cl-rich phase(s) within

GRA 06129 which, due to the nucleogenic reaction during irradiation, decays into two argon species. During irradiation, ^{37}Cl captures a neutron, becoming ^{38}Cl, which will β-decay to ^{38}Ar at a half-life of 37.3 min. The release patterns are not the same for the three aliquots, suggesting different Cl-rich components and proportions in each aliquot. Consequently, and due to the difficulty in determining the spallation-derived ^{38}Ar$_{Ca}$, no cosmic ray exposure ages were calculated. In the preceding sections, it was mentioned
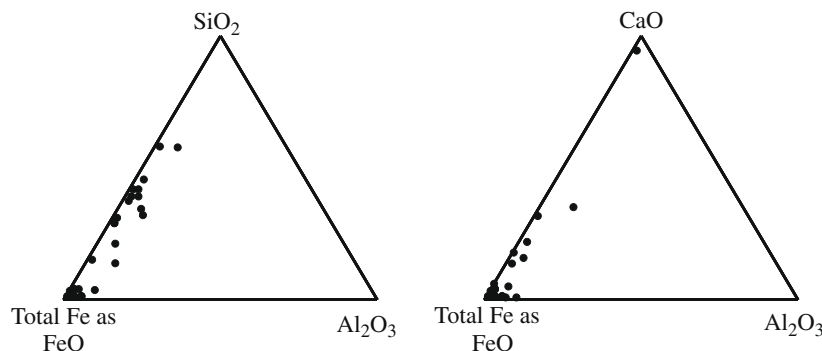
Fig. 9. Electron microprobe analyses of alteration in GRA 06129,23 graphically represent in FeO–CaO–Al$_2$O$_3$ (wt.%) and FeO–SiO$_2$–Al$_2$O (wt.%).

that GRA 06129 showed the existence of low-temperature alteration products and Cl-apatite. It is likely that both phases are the culprits for the high $^{38}Ar/^{36}Ar$ values observed at intermediate and high temperature steps. However, due to the high Cl content of the apatite and the slight increase in Ca at the intermediate temperature heating steps, it is likely that this phase is the major contributor for this excess ^{38}Ar which was released over most of the intermediate and high temperature steps of aliquots 2 and 3.

In a three isotope diagram (Fig. 13) all three samples show excess ^{129}Xe from decay of ^{129}I. Sample 330 also shows evidence of fissiogenic xenon; although the isotopic data are consistent with either ^{238}U or ^{244}Pu as the parent, ^{244}Pu dominates production of fission xenon at times consistent with the presence of live ^{129}I and the Ar–Ar plateau age (Turner et al., 2007).

Concentrations of the various xenon components (fissiogenic, iodogenic, trapped) vary considerably among these three small samples. The composition of the trapped xenon component is consistent with Q-Xenon (Busemann et al., 2000) with evidence of minor modification by a spallation signal in the light isotopes ($^{128-131}Xe$); there is no evidence of a significant contribution of xenon from the terrestrial atmosphere as might be expected from significant terrestrial weathering. Q-Xenon is typical of primitive chondritic meteorites; its presence here demonstrates retention of a significant signature of extreme volatiles from a presumed primitive parent. Concentrations of trapped xenon components (fissiogenic, iodogenic, trapped) are in a range similar to that observed among milligram samples of lodranites ($10^8–10^{10}$ atoms ^{132}Xe g^{-1} (Crowther et al., 2009) and significantly higher than those reported for evolved achondrites, which also tend to exhibit little or no iodogenic ^{129}Xe (Patzer et al., 2003; Busfield et al., 2008). Assuming iodine was trapped with $^{129}I/^{127}I \sim 10^{-4}$, ^{129}Xe concentrations of $<10^{10}$ atoms g^{-1} (Table 5) correspond to iodine concentrations <20 ppb, consistent with the values obtained for evolved achondrites (Busfield et al., 2008).

In sample 330, fissiogenic xenon is released at slightly lower temperatures than iodogenic ^{129}Xe. Merrillite is a host phase of fission xenon from plutonium decay in Acapulco (Nichols et al., 1994) and we suggest it is implicated here; it seems that the mineral that hosted ^{129}I is somewhat

more retentive of xenon. Pyroxenes and feldspars have both been demonstrated to be retentive iodine carriers (Brazzle et al., 1999; Gilmour et al., 2000), though the distribution among our three samples and the observation that a single step in the analysis of 231 contributed 70% of the iodogenic ^{129}Xe in this sample suggests a contribution from a minor phase, perhaps halogen-rich apatite or alteration products.

3.6. $^{26}Al–^{26}Mg$ isotope measurements

The Al/Mg ratios and $\Delta^{26}Mg$ of GRA 06129 whole rock and plagioclase mineral separates are given in Table 6 and the $^{26}Al–^{26}Mg$ isochron plot is shown in Fig. 14. The whole rock and mineral separates all have uniform excesses of radiogenic ^{26}Mg ($\Delta^{26}Mg$) regardless of their Al/Mg ratios, indicating that Mg isotopes were equilibrated in this meteorite subsequent to the complete decay of ^{26}Al. The slope of the $^{26}Al–^{26}Mg$ isochron (Fig. 14) is not resolved from zero and corresponds to an upper limit on the $^{26}Al/^{27}Al$ ratio of 2.08×10^{-8} at the time of last equilibration of Mg isotopes. However, the initial $^{26}Al/^{27}Al$ ratio at the time of the major fractionation event that established the Al/Mg ratio in the GRA 06129 whole rock (presumably plagioclase accumulation and crystallization) may be inferred from the Mg isotopic composition of the GRA 06129 whole rock which records a $\Delta^{26}Mg$ value of 0.080 ± 0.009‰. Assuming that GRA 06129 originated from a chondritic source reservoir, i.e., characterized by an initial $\Delta^{26}Mg$ of -0.001 ± 0.002‰ and $^{27}Al/^{24}Mg = 0.101 \pm 0.004$ (Thrane et al., 2006), a model initial $^{26}Al/^{27}Al$ ratio of $2.19 \pm 0.25 \times 10^{-6}$ is inferred at the time of its crystallization.

3.7. Fourier transform infrared spectroscopy

The micro-FTIR transmission spectra of the fine-grain alteration along grain boundaries and within fractures are identical to the spectra from powders in the 10, 000–5000 cm^{-1} range. The thin section spectra were complicated by the epoxy and glass slide in the 5000–650 cm^{-1} range. In the powder samples, a band at ~3420 cm^{-1} may indicate adsorbed H$_2$O and a shoulder at ~3250 cm^{-1} may indicate molecular H$_2$O, but only extremely weak bands are observed at 5200 and 1650 cm^{-1} for molecular H$_2$O and no bands are observed for OH (at 4500 cm^{-1}). The alteration

Table 2
Major and trace element analyses of bulk GRA06129 (1 g sample, 2 splits). Trace element concentrations are in parts per million. All elements determined by ICP-MS except S.

	Split 1	Split 2	Average	Normative mineralogy[c]	
SiO_2	50.14	49.99	50.06	Plagioclase	48.86
TiO_2	0.07	0.07	0.07	Orthoclase	1.48
Al_2O_3	15.18	15.13	15.15	Nepheline	11.69
Fe_2O_3[a]	12.33	12.34	12.33	Diopside	19.24
MnO	0.10	0.10	0.10	Olivine	7.48
MgO	2.65	2.65	2.65	Ilmenite	0.13
CaO	6.20	6.24	6.22	Magnetite	1.78
Na_2O	7.50	7.53	7.51	Apatite	0.44
K_2O	0.26	0.25	0.25	Chromite	0.01
P_2O_5	0.19	0.19	0.19	Pyrite	4.88
S	2.30	2.30	2.30		
LOI	3.65	3.65	3.65		
Total[b]	98.26	98.13	98.20		
Sc	5.17	5.32	5.2		
V	18.58	15.71	17.11		
Cr	83.86	79.99	81.90		
Co	288.9	306.0	297.4		
Ni	2158	2272	2215		
Cu	35.6	34.64	35.1		
Ga	53.84	56.30	55.1		
Rb	1.59	1.57	1.58		
Sr	54.50	57.40	55.95		
Y	3.95	3.85	3.90		
Zr	3.69	5.28	4.49		
Nb	0.16	0.15	0.15		
Sn	0.15	0.11	0.13		
Cs	0.03	0.03	0.03		
Ba	23.46	26.16	24.81		
La	0.94	0.90	0.92		
Ce	2.29	2.17	2.23		
Pr	0.32	0.30	0.31		
Nd	1.52	1.46	1.49		
Sm	0.48	0.47	0.47		
Eu	0.48	0.45	0.47		
Gd	0.54	0.48	0.51		
Tb	0.12	0.10	0.11		
Dy	0.81	0.68	0.74		
Ho	0.16	0.15	0.16		
Er	0.45	0.40	0.42		
Tm	0.06	0.05	0.05		
Yb	0.35	0.33	0.34		
Lu	0.05	0.04	0.04		
Hf	0.42	0.80	0.61		
Ta	0.02	0.01	0.01		
W	0.11	0.09	0.10		
Pb	0.28	0.08	0.18		
Th	1.30	1.23	1.27		
U	0.03	0.02	0.02		

[a] Total Fe calculated as Fe_2O_3.
[b] Total does not include S as it represents a portion of the LOI (loss on ignition).
[c] Normative mineralogy (wt%) calculated from average assuming a Fe^{3+}/(total Fe) = 0.10.

minerals in our sample of the powder do not show bands observed for sulfates or carbonates suggesting that those minerals are below detection if present. Neither do we observe distinctive bands for common clay minerals like kaolinite or smectite group minerals (cf. nontronite; Sunshine et al., 2009). Instead, bands between 1140 and 830 cm^{-1} are most consistent with bands commonly observed in amorphous material (e.g., van der Marel and Beutelspacher, 1976). Bands diagnostic of hematite or goethite are absent near 8000 cm^{-1}, therefore those minerals are unlikely or below detection. Based on the near- and mid-IR analysis and other chemical evidence (e.g., above,; Fig. 9; Zeigler et al., 2008; Treiman et al., 2008), it is most likely that the alteration is dominantly an amorphous admixture
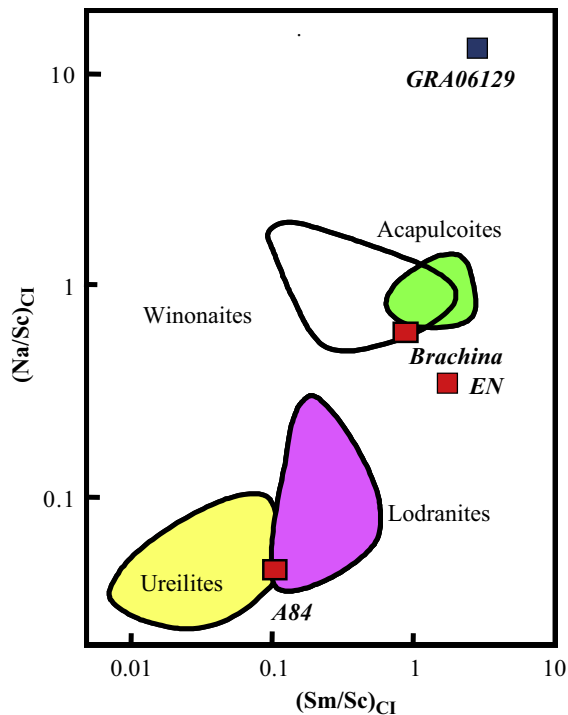
Fig. 10. Plot of Na/Sc vs Sm/Sc for bulk GRA 06129. Also included in this plot are fields for ureilites, winonaites-IAB silicates, acapulcoites and lodranites and points (red squares) representing individual brachinites such as brachina, ALH 84025 (A84), and eagles nest (EN) (modified from Mittlefehldt et al., 1998). Ratios normalized to CI chondrite (Anders and Grevesse, 1989).

containing nanophase Fe^{3+}–O–H phases, amorphous silicates and Ca-phases, with minor sulfate and chloride. These findings suggest that alteration took place at near-neutral to very slightly acidic conditions.

3.8. Magnetic properties

The natural remanent magnetization (NRM) moment of the UNM specimen is 1.94×10^{-6} emu (intensity of 16.08×10^{-6} Am^2/kg). Progressive alternating field demagnetization of the GRA specimen measured indicates that the meteorite NRM may contain at least two components. Alternating-field (AF) demagnetization to 95 mT randomizes less than 50% of the NRM; at higher peak fields demagnetization behavior is more erratic. A possible higher coercivity component only partially responds to AF demagnetization and thermal demagnetization of NRM. Intensity of anhysteretic remanent magnetization (ARM) is about 81.0×10^{-6} Am^2/kg and over a factor of 6 higher than NRM. The intensity of ARM as well as AF demagnetization response to ARM indicates that a considerable fraction of moderate coercivity phases is present that does not contribute to the NRM. Acquisition of an isothermal remanent magnetization shows nearly complete saturation at about 3.0 T, and backfield DC demagnetization of near-saturation IRM yields an estimate of coercivity of remanence of about 280 mT. The near saturation IRM intensity is about 2970×10^{-6} Am^2/kg, and yields an ARM/SIRM ratio of

approximately 0.027. Comparison of AF demagnetization of ARM and near-saturation IRM suggests the presence of fine, single domain to pseudo single domain ferrimagnetic particles in the specimen. In addition, the very low crossover value ($R < 0.1$) for IRM acquisition and AF demagnetization of near saturation IRM at least suggests the possibility of strongly interacting magnetic phases (Cisowski, 1981; Moskowitz et al., 1993). Thermal demagnetization of three component IRM suggests that the magnetization is carried by high-coercivity phases with laboratory unblocking temperature intervals that center on $\sim$350, $\sim$570, and $\sim$675 °C that are likely pentlandite, a Fe–Ni metal, and hematite, respectively. Thermal demagnetization of both the high ($>$3.0 T) and intermediate (0.3 $<$ H $<$ 3.0 T) coercivity components also suggests the possibility of the thermal destruction of iron hydroxide phases between about 100 and 200 °C. The intermediate and lowest field (coercivity) ($<$0.03 T) components show a $\sim$complete unblocking below about 570 °C, and this response is consistent with the observed occurrence of Fe, Ni metal. Notably, the response to thermal demagnetization of three component IRM does not suggest the generation of abundant new magnetic phases that could be reflected in an increase in the intensity of one of the components during progressive heating. Magnetic properties of GRA are graphically represented in electronic annex EA-4 through EA-7.

4. DISCUSSION

4.1. Conditions of crystallization and metamorphism

Most of the primary igneous textures and mineral compositions have reequilibrated at subsolidus temperatures. This is reflected in features such as pyroxene exsolution, granoblastic texture, generally homogeneous mineral compositions, and diffusion profiles adjacent to olivine–chromite and chromite–ilmenite interfaces. Therefore, all of the estimates of temperature and oxygen fugacity reflect metamorphic conditions and not necessarily conditions of magmatic crystallization.

Because of the fairly low "others" component in the pyroxene, the pyroxene thermometry of Lindsley (1983) may be used to approximate the temperature under which the pyroxene pairs last equilibrated. Using this thermometer, the temperature of pyroxene equilibration is approximately 670 ± 50C and is consistent with extensive post-crystallization metamorphism. The ferric iron content of pyroxene in GRA implies an oxygen fugacity (fO_2) that is more oxidizing than the Moon (one log unit below the iron–wustite buffer (IW-1)) as lunar pyroxenes contain no ferric iron.

Ferric iron contents in chromite and ilmenite were determined assuming stoichiometry, where Fe_2O_3 contents were adjusted to give cation sums of 3 for chromite and 2 for ilmenite. This process resulted in totals within acceptable limits for the majority of analyses. Chromite composition is expressed in terms of endmembers: ulvöspinel, Usp = molar $2Ti/(2Ti + Cr + Al + Fe^{3+})$; spinel, Sp = molar $Al/(2Ti + Cr + Al + Fe^{3+})$; chromite, Chr = molar $Cr/(2Ti + Cr + Al + Fe^{3+})$; and magnetite, Mt = molar $Fe^{3+}/(2Ti + Cr + Al + Fe^{3+})$. Oxygen fugacity calculations

Table 3
Isotopic compositions of hydrogen, carbon, oxygen, and sulfur in GRA 06129. Isotopic composition of hydrogen and carbon are from volatiles released from GRA 06129 during step heating. Values in shaded fields have high errors due to the very low amount of water or C released at these higher temperatures (T). n.d., not determined; m, minutes; ramping refers to the time driving the sample from one temperature to a higher temperature.

Cycle	δD (‰ vs SMOW)	T	Time (min)	Area
Hydrogen (197 mg sample)				
1		200 °C	5	
2	−153	200 °C	15	1009
3	−121	350 °C	15	150.1
4	−39	500 °C	15	20.6
5	21	800 °C	15	4.4
6	66	1015 °C	20	2.2
Carbon (188 mg sample)				
	$\delta^{13}C$ (‰ vs PDB)			
1	−13.98	145 °C	4	1.99
2	−26.36	Ramping	4	18.42
3	−25.72	315 °C	4	17.10
4	−23.91	315 °C	6	7.65
5	−25.72	317 °C	5	5.06
6	−25.97	Ramping	4	50.66
7	n.d.	467 °C	4	n.d
8	−19.28	472 °C	7	7.82
9	n.d.	Ramping	5	5.00
10	n.d.	614 °C		

Oxygen (2 mg for each split)			*Sulfur (50 mg for each split)*	
	$\delta^{17}O$ (‰ vs SMOW)	$\delta^{18}S$ (‰ vs CDT)		
	$\delta^{18}O$ (‰ vs SMOW)			
Split 1-O	2.82	5.74	Split 1-S	−1.05
Split 2-O	2.88	5.92	Split 2-S	−0.55
Split 3-O	2.85	5.83		

involving the Fe–Ti oxide mineral equilibrium were carried out according to the formulation of Ghiorso and Sack (1991). Equilibration temperatures of olivine–chromite
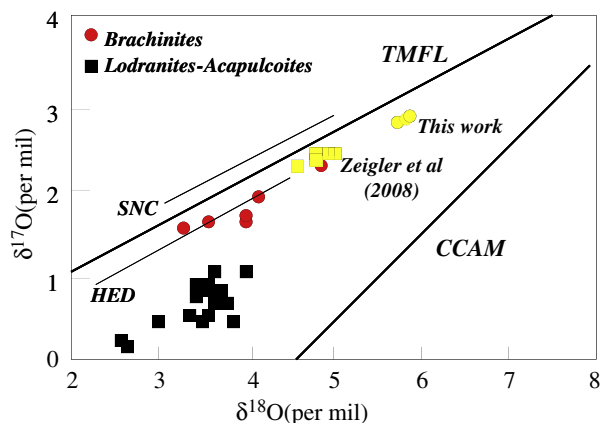

Fig. 11. Oxygen isotope characteristics for GRA 06128 (Zeigler et al., 2008) and GRA 06129 (this work; Zeigler et al., 2008). Additional O isotope data has been reported by Day et al. (2009). The terrestrial mass fractionation line (TMFL), carbonaceous chondrite anhydrous mineral line (CCAM), SNC, and HED fields, and individual brachinite and lodranite–alcopocoite points are shown for comparison.

(ol–sp) pairs were determined using the geothermometer of Sack and Ghiorso (1991a). The olivine–pyroxene–chromite (Ol–Px–Sp) method of oxybarometry was applied according to the procedure outlined by Herd et al. (2002) which utilizes the equilibration temperature from ol–sp geothermometry and the activity of Fe_3O_4 in chromite determined using the MELTS Supplemental Calculator (Sack and Ghiorso, 1991a,b). The uncertainty of this method is ±0.5 log units (one sigma) according to Wood (1991).

Selection of equilibrium assemblages for Ol–Px–Sp oxybarometry was carried out primarily on the basis of spatial association (Figs. 1 and 2). Some compositional zoning in chromite was observed; for example, chromite adjacent to the highest Mg# olivine (Fo_{44}) (Figs. 1, 2, and 6) ranges in composition from $Chr_{43}Sp_8Usp_{49}Mt_0$ to $Chr_{42}Sp_8Usp_{47}Mt_3$. Calculation of oxygen fugacity using the Ol–Px–Sp method yields a range of estimates that depends on the chromite composition, as the olivine and pyroxene compositions vary little within the meteorite. Applying the criterion of Goodrich et al. (2003) that the least equilibrated chromite has the highest Cr′ (molar Cr/[Cr + Al]) and lowest Fe′ (molar Fe/[Fe + Mg]), in this case corresponding to $Chr_{43}Sp_8Usp_{49}Mt_0$, and that it is in equilibrium with the most magnesian olivine (Fo_{44}), and the most Mg-rich and Ca-poor orthopyroxene ($Wo_2En_{54}Fs_{44}$), calculation by this method yields T = 868 °C and oxygen fugacity slightly below the Iron-Wüstite (IW) buffer, i.e.,

Table 4
Summary of ^{40}Ar–^{39}Ar measurements for three bulk fragments of GRA 06129.

GRA06129 aliquot	Weight (mg)	Plateau age (Ga)	Slope age (Ga)	^{39}Ar release (%)	Total ^{38}Ar (mol $\times 10^{-16}$)
1	1.85	4.425 ± 0.016	4.424 ± 0.032	35	1.80 ± 0.03
2	2.95	4.473 ± 0.016 2.673 ± 0.038[a]	4.460 ± 0.008	89	1.50 ± 0.01
3	2.30	4.467 ± 0.018 3.845 ± 0.034[a]	4.463 ± 0.009	92	2.27 ± 0.01

[a] Minimum apparent age during IR-laser step heating corresponding to maximum age for an event that caused the partial re-setting observed at low-temperature steps. The preferred age for this resetting is $\leqslant 2.673 \pm 0.038$ Ga which is not fully shown in the release spectrum of aliquot-3 due to differences in the step heating schedule; the step heating schedule for aliquot-2 began at lower temperature than that for aliquot-3.
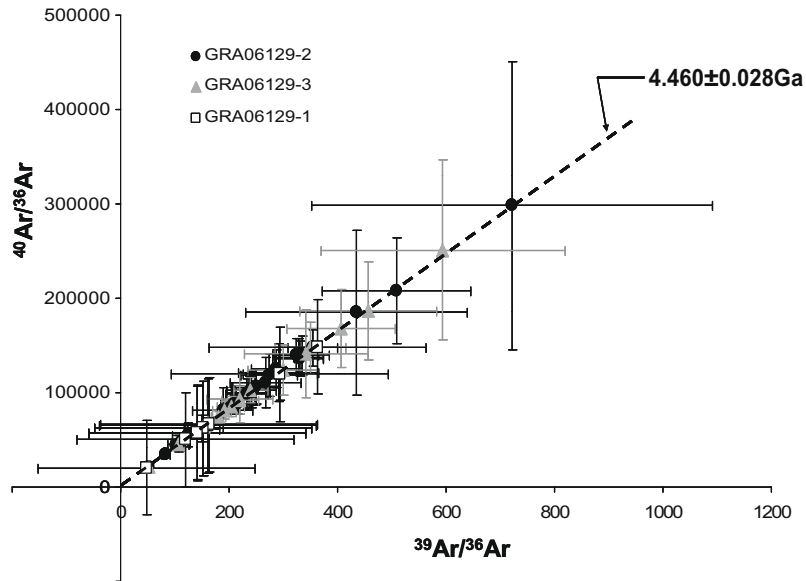

Fig. 12. $^{40}Ar/^{36}Ar$ vs. $^{39}Ar/^{36}Ar$ for the three bulk aliquots of meteorite GRA 06129. The correlation lines were acquired over all the data obtained for the three aliquots.

$fO_2 = IW - 0.1$ (± 0.5). These estimated temperature conditions of crystallization my reflect the three phases underwent re-equilibration or that >2% water was associated with crystallization. The former is more consistent with the textures exhibited by GRA. The presence of Fe–Ni metal in the rock and a small percentage of Fe^{3+} in Fe–Mg silicates are notable, and are consistent with conditions close to or slightly above the IW buffer.

Chromite compositions range up to Mt = 3.5%, and may represent the effects of subsolidus equilibration under slightly more oxidizing conditions. Utilizing the most Mt-rich chromite ($Chr_{42}Sp_8Usp_{47}Mt_3$) with the predominant olivine composition (Fo_{40}) and a slightly more Fe-rich orthopyroxene ($Wo_2En_{53}Fs_{45}$) yields $T = 733\,°C$ and $fO_2 = IW + 2.0$ (± 0.5) using the Ol–Px–Sp method. This estimate reflects the higher Mt content of the chromite, since the oxybarometer is relatively insensitive to olivine or pyroxene compositions, and may be representative of the conditions of subsolidus re-equilibration.

Application of the Fe–Ti oxide oxybarometer to assemblages in GRA 06129 is problematic; the high V concentrations of chromite in GRA 06129 (up to 3 wt% V_2O_3) are well outside the range used in the development of the various formulations of this oxybarometer, including Ghiorso

and Sack (1991) (see Herd, 2008, for a review). As such, even spatially co-located chromite–ilmenite pairs cause convergence errors during calculation. No ferric iron is present in ilmenite on the basis of stoichiometry, consistent with low oxygen fugacity conditions. Calculation using low-Mt chromite yielded convergence errors; calculation using the highest-Mt chromite ($Chr_{42}Sp_8Usp_{47}Mt_3$) with ilmenite containing 6% geikielite ($MgTiO_3$) and 1% pyrophanite ($MnTiO_3$) yields $T = 962\,°C$ and $fO_2 = IW + 1.1$ according to the Ghiorso and Sack (1991) formulation. This estimate represents an upper limit, since it utilizes the composition of chromite that we previously interpreted to be the result of subsolidus equilibration.

4.2. Chronology of GRA 06128 and GRA 06129

4.2.1. Age of early crystallization

Preliminary phosphate Pb–Pb ages obtained from GRA are imprecise, but ancient (4.4–4.6 Ga) (Ash et al., 2008) and therefore suggest these meteorites represent a melting event early in the history of the solar system. From the $^{26}Al/^{27}Al$ ratio inferred in Section 3.6 for the time of major Al/Mg fractionation, we can infer a ^{26}Al–^{26}Mg model age relative to the D'Orbigny angrite (Amelin, 2008a;
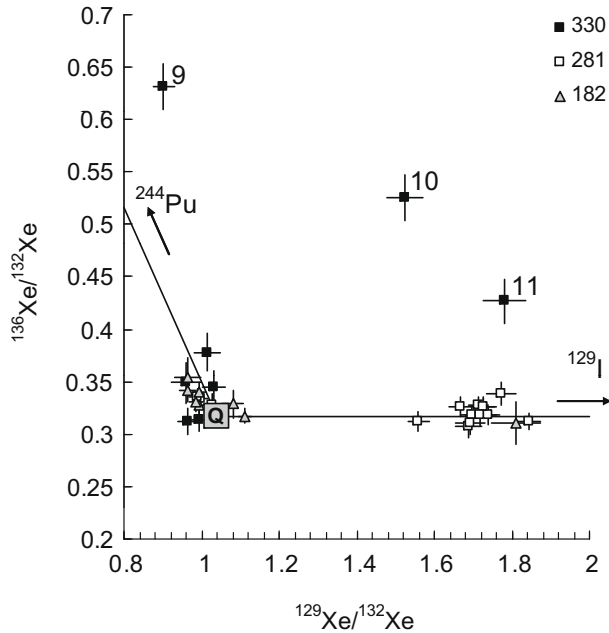
Fig. 13. Data from xenon isotopic analyses of three grains, sample numbers correspond to mass in micrograms. Samples 182 and 281 are consistent with modification of Q-xenon (Busemann et al., 2000) by in-growth of ^{129}Xe from decay of ^{129}I (half life 16 Myr), 330 also shows evidence of xenon produced by fission of ^{244}Pu. Data from the final three releases from 330 are labeled with the step number. Data from releases with less than 10,000 atoms of ^{132}Xe (<10× blank) are not plotted.

Table 5
Contents in 10^9 atoms g^{-1} of trapped ^{132}Xe, fissiogenic ^{136}Xe from ^{244}Pu and ^{129}Xe from decay of ^{129}I. Data in parentheses exclude a single dominant release from sample 231.

Sample	^{132}Xe	^{136}Xe (Pu)	^{129}Xe (I)
330	0.9	0.076	0.1
231	19.4	0.009	10.4
	(10.2)	(0.009)	(3.3)
182	12.3	0.030	0.6

Table 6
Al–Mg isotopic data for GRA 06129.

Sample[a]	^{27}Al/^{24}Mg[b]	Δ^{26}Mg (‰)	±2SE[c]	n[d]
WR	5.25	0.080	0.009	12
PL-1	256.10	0.088	0.029	3
PL-2	85.82	0.084	0.018	7

[a] WR, whole rock; PL, plagioclase.
[b] Errors (2σ) in the 27Al/^{24}Mg ratios are ±2%.
[c] Errors in the Mg isotope ratios are twice the standard error.
[d] Number of repeat measurements.

Fig. 14. ^{26}Al–^{26}Mg isochron plot for GRA 06129.

Spivak-Birndorf et al., 2009) of 4565.9 ± 0.3 Ma. This is most likely the age of plagioclase accumulation and crystallization and is not related to the age of later metamorphism. Chronological investigations of achondritic meteorites indicate that melting and differentiation of planetesimals began as early as 2–5 Ma after the formation of the refractory cal-
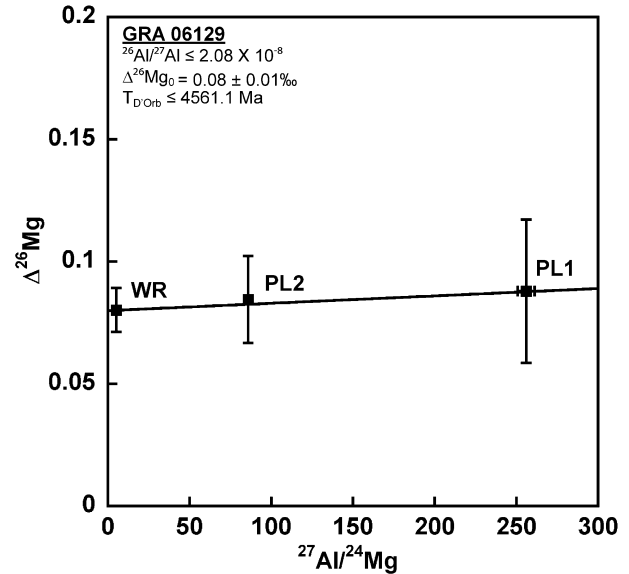
cium–aluminum-rich inclusions (CAIs) that are thought to be the earliest solids to form in the solar nebula (Wadhwa et al., 2006; Connelly et al., 2008; Jacobsen et al., 2008; Bouvier and Wadhwa, 2009) and possibly continued until planetary-scale events were recorded on the Moon and Mars between 25 and 250 Ma (Mittlefehldt et al., 1998; Wadhwa et al., 2006). How does the age of crystallization for GRA fit within the context of the earliest stages of planetesimal differentiation and magmatism?

Primitive achondrites, such as winonaites, brachinites, and acapulcoites–lodranites exhibit magmatic textures and have bulk compositions that are close to those of chondrites (McCoy et al., 1997; Mittlefehldt et al., 1998). These meteorites best illustrate the linkage between chondrites and initial stages of melting on a planetesimal. Chronological studies of acapulcoites–lodranites (Prinzhofer et al., 1992; Zipfel et al., 1996; Pellas et al., 1997; Amelin and Pravdivtseva, 2005) indicate that the incipient melting events represented by these meteorites occurred within 10 million years of the first solids in the solar system. The current best estimate of the U–Pb age (from phosphates) of Acapulco is 4555.1 ± 1.3 Ma (Amelin and Pravdivtseva, 2005); ^{53}Mn–^{53}Cr isotope systematics for Acapulco (Zipfel et al., 1996) translate to an age of 4556.5 ± 1.1 Ma relative to D'Orbigny (Glavin et al., 2004; Amelin, 2008a), consistent with the U–Pb age. The Mn–Cr age of Brachina (also relative to D'Orbigny) is 4565.3 ± 0.6 Ma (Wadhwa et al., 1998) indicating that magmatism on the Brachina parent body occurred within ~2 to 3 Ma after the formation of CAIs.

The howardites, eucrites, and diogenites (HEDs) represent a much more extensive period of asteroidal magmatism than represented by the primitive achondrites. In the HEDs, the relationship between magmatism and the sources experiencing melting (presumably near-chondrite material) are far more obscure due to both the more extensive melting and a protracted post-crystallization thermal history. Evidence for the presence of short-lived radionuc-
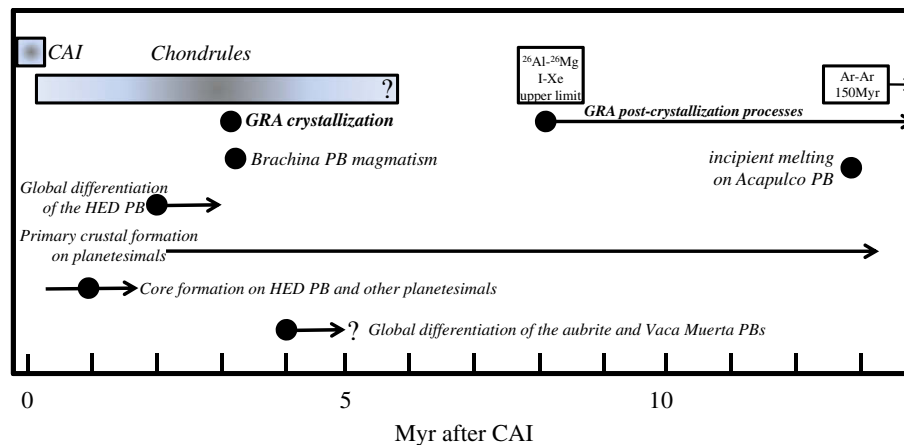
Fig. 15. Relationship between events determined for GRA and events in the early solar system (after Wadhwa et al., 2006).

lides such as ^{26}Al, ^{53}Mn, and ^{60}Fe (e.g., Shykolyukov and Lugmair, 1993; Lugmair and Shykolyukov, 1998; Nyquist et al., 2003) has been found in non-cumulate eucrites and has been interpreted as indicating that crustal formation on 4 Vesta (and other similar parent bodies) began within 2–3 Ma of CAI formation and extended to ∼10 Ma thereafter (Wadhwa and Russell, 2000 Wadhwa et al., 2006). Finally, based on ^{182}Hf–^{182}W systematics of a variety of differentiated meteorites (including iron meteorites), it has been suggested that extensive melting on planetesimals leading to core formation began almost contemporaneously with CAI formation (Kleine et al., 2005; Markowski et al., 2006; Qin et al., 2008).

The relationship of the crystallization age inferred here for GRA (based on its Al–Mg systematics) to other thermal events in the early solar system is represented in Fig. 15. The GRA melting-crystallization event appears to be contemporaneous with brachinite parent body magmatism and silicate differentiation on the HEDs and angrite parent bodies. The GRA crystallization appears to predate asteroidal incipient melting represented by the acapulcoites and lodranites, but this observation could be partially a result of the comparison of various chronometers and post-melting metamorphism experienced by the acapulcoites (McCoy et al., 1997).

A further interesting observation is that the timing of asteroidal melting represented by GRA and other meteorites appears to overlap with that of chondrule formation events (Fig. 15). One interpretation is that many of the younger ages of the chondrules that were derived from Al–Mg isotopic measurements reflect metamorphic reequilibration (>450 °C) after parent body accretion. Alternatively, accretion and differentiation of planetesimals occurred contemporaneously with chondrule formation processes within different portions of the asteroid belt. This is supported by recent reports of high precision Pb–Pb ages of CAIs, chondrules and some achondrites (Amelin et al., 2002; Amelin, 2008a,b; Connelly et al., 2008; Jacobsen et al., 2008; Wadhwa et al., 2006) as well as the Hf–W isotope systematics in CAIs, achondrites and iron meteorites (Kleine et al., 2005; Markowski et al., 2006, 2007; Burkhardt et al., 2008; Qin et al., 2008).

4.2.2. Age of post-magmatic crystallization events

There are numerous events that are recorded in this meteorite that occurred at near solidus conditions or clearly post-dated magmatic crystallization. These events include (1) subsolidus reequilibration of magmatic phases and/or the formation of the granoblastic texture, (2) reaction between primary magmatic phases such as merrilite and pyroxene and either a residuum melt or fluid phase, and (3) alteration along grain boundaries and within fractures that reflect low temperature alteration on either (or both) the parent body or Earth. The primary crystallization age of ∼4566 Ma inferred here from the Al–Mg systematics for GRA is ∼106 million years older than the 4420 Ma Ar–Ar age calculated from the slope of the isochron in Fig. 12. This complete K–Ar system reset age may correspond to the age of metamorphism and/or the formation of the granoblastic texture. This event is not uniquely preserved in this meteorite as it has also been observed in HED-achondrites and chondrites (for a complete list see Bogard (1995) and Swindle et al. (2009) and references therein). A more recent thermal event at ∼2.67 Ga, only partially reset the K–Ar system as observed in the initial ∼10% ^{39}Ar release (Fig. 12). Similar partial reset ages at 2.5–2.6 Ga have been reported for other meteorites such as the impact melt in H-chondrite NWA 2457, Johnstown diogenite and Netschaëvo IIE (Balacescu and Wänke, 1977; Niemeyer, 1980; Fernandes et al., 2006). Also, although Al/Mg fractionation in GRA occurred while ^{26}Al was extant, the internal ^{26}Al–^{26}Mg isotope systematics of GRA (Fig. 14) indicate that this chronometer was reset at a later time, which may be contemporaneous with the age recorded by the Ar–Ar system. The ^{26}Al–^{26}Mg data are consistent with post-crystallization metamorphism and correspond to an upper limit of 4561.1 Ma for the timing of this event (Fig. 14). The presence of ^{129}Xe* demonstrates (Fig. 13) that the I–Xe system records closure substantially earlier than the Ar–Ar plateau age, perhaps associated with the event that reset the Al–Mg isochron.

4.3. Planetary body of origin

The ancient crystallization age for the GRA meteorites indicates that they represent products of early melting on

an asteroid rather than a large planetary body (i.e., Earth, Moon, Mars). Numerous investigators have discussed the planetary body of origin for this meteorite. Zeigler et al. (2008) was the first to suggest that the brachinite parent was geochemically related to the parent body of GRA. Shearer et al. (2008) suggested that GRA was derived from a parent body with similar geochemical characteristics and thermal history as the brachinite parent body. Mineral chemistries, oxygen isotopic composition, magnetic properties, and conditions of crystallization–metamorphism all yield insights into the nature of the planetary body from which this meteorite was derived.

In contrast to the initial O isotopic composition reported for this pair of meteorites, oxygen isotopic compositions are not consistent with an origin in the Earth–Moon system. The $\Delta^{17}O$ value of -0.18 is similar to a number of achondrites such as the eucrites, howardites, diogenites, angrites, mesosiderites, pallasites, and brachinites (Clayton and Mayeda, 1996). In all cases, the $\delta^{18}O$ values of these different classes are lower than those measured for GRA. For example, the brachinites have a $\delta^{18}O$ values as high as 4.91‰. Our measured $\delta^{18}O$ values for GRA average 5.8‰ (Fig. 11), although others have reported $\delta^{18}O$ values ranging from 4.5‰ to 5.0‰ (Zeigler et al., 2008; Day et al., 2009). The differences among the GRA measurements can be attributed to heterogeneities associated with different mineral proportions analyzed. The $\Delta^{17}O$ value is unaffected by preferential analysis of one phase relative to another, as long as all phases are in isotopic equilibrium.

Estimates of fO_2 made above indicate that the subsolidus reequilibration of the GRA mineral assemblage occurred at conditions of between $IW - 0.1$ and $IW + 1.1$. This is more oxidizing than expected for the Moon $(IW - 1)$, and the parent bodies of the HED meteorites $(\approx IW - 1)$, aubrites $(\approx IW - 5)$, acapulcoites–lodranites $(\approx IW - 2)$, and winonaites/IAB silicate inclusions $(\approx IW - 2)$ (Mittlefehldt et al., 1998; Benedix et al., 1998; Wadhwa, 2008) but too reducing for most environments on Earth. Both the angrites and brachinites appear to reflect similar fO_2 conditions as those calculated for GRA. McKay et al. (1994) estimated the magmatic redox conditions for the angrites to be close to $IW + 1$. Nehru et al. (1992, 1996) concluded that the oxidized mineral assemblage attributed to the brachinites was a result of heating and partial melting of CI-like material accompanied by oxidation via the reaction: $MgSiO_3$ (orthopyroxene) $+ Fe$ (metal) $+ 0.5O_2 \Leftrightarrow (Mg,Fe)_2SiO_4$ (olivine). Melts removed (and thus far unsampled) during this episode of brachinite parent body melting should reflect this oxidation reaction. Whether or not these melts are represented by GRA, this reaction may account for the fO_2 conditions under which GRA crystallized.

The Fe/Mn ratios of mineral phases such as olivine and pyroxene have been used to determine planetary origins of meteorites (Karner et al., 2003). However, many of these systematics are defined by basaltic lithologies with few metamorphic features, unlike GRA. Nevertheless, the Fe/Mn of olivine and pyroxene in GRA are consistent with some of the observations made above. The Fe/Mn ratios in olivine from GRA overlap with those of terrestrial sam-

ples and brachinites and are strikingly different from the acapulcoites–lodranites (Fig. 16). Further, the Fe/Mn ratios of pyroxenes from GRA overlap with those from terrestrial samples (brachinite data was not available) and are distinct from those of HED meteorites (Fig. 16). The concentrations of Ni and Co in olivine appear to be consistent with the observations based on Fe/Mn ratios. Both Ni and Co contents in GRA are substantially higher than those observed in olivine-bearing lithologies (diogenites) from the HED parent body and in a meteorite (QUE 93148) hypothesized to represent the mantle from either the HED or pallasite parent body (Fig. 7). The Ni concentrations in olivine from brachinites as determined by electron microprobe (0.05 wt.% NiO) are intermediate between the assemblages representing HED magmatism and GRA (Nehru et al., 1992, 1996). Differences in Ni in olivine from these different planetary environments probably reflect both differences in fO_2 (Nehru et al., 1992, 1996; Wadhwa, 2008) and sulfide–metal segregation. However, the higher ratio of the Ni content in metal to that in olivine in QUE 93148 ($Ni_{metal}/Ni_{olivine} > 1000$) compared to GRA ($<800$) indicates fO_2 does play a role.

A large body of geochemical evidence suggests that the GRA mineral assemblage was generated on a parent body with many fingerprints similar to the brachinite parent body. Although the brachinites are dominated by olivine and pyroxene and are therefore mineralogically distinct from GRA, both lithologies have similar oxygen isotopic compositions, similar Fe/Mn ratios and Ni contents in their olivine, and were produced under comparable fO_2 conditions. Further comparisons of Ni and Co concentrations in olivine between GRA and brachinites seem warranted to further explore a possible petrogenetic linkage. The thermal history implied by the chronology discussed in the earlier sections indicates that GRA was derived from a planetary body that experienced and preserved episodes of early planetesimal melting similar to the melting history experienced by the brachinite parent body.

Assuming that the bulk of the magnetic phases in the 120 mg specimen of GRA investigated are not products of terrestrial weathering, we interpret the magnetic data reported here to indicate that the process of NRM acquisition in the specimen was a very inefficient one, in that a considerable fraction of the magnetic phases do not contribute to the NRM. How the NRM acquisition process may be related to the presence of a relatively strong (e.g., comparable to the Earth's surface field) or weak magnetic field is difficult to assess given the present data.

4.4. Origin of high-temperature mineral assemblage

Unlike GRA, brachinites are relatively fine-grained, olivine bearing, ultramafic rocks that are essentially dunites and peridotites. The brachinites and other primitive achondrites (such as acapulcoites, lodranites, ureilites, winonaites) are thought to represent the extensive metamorphism of chondritic precursors resulting in varying degrees of melting and melt extraction (Nehru et al., 1992, 1996; McCoy et al., 1997; Benedix et al., 1998; Mittlefehldt et al., 1998). The mineralogy and geochemistry of these
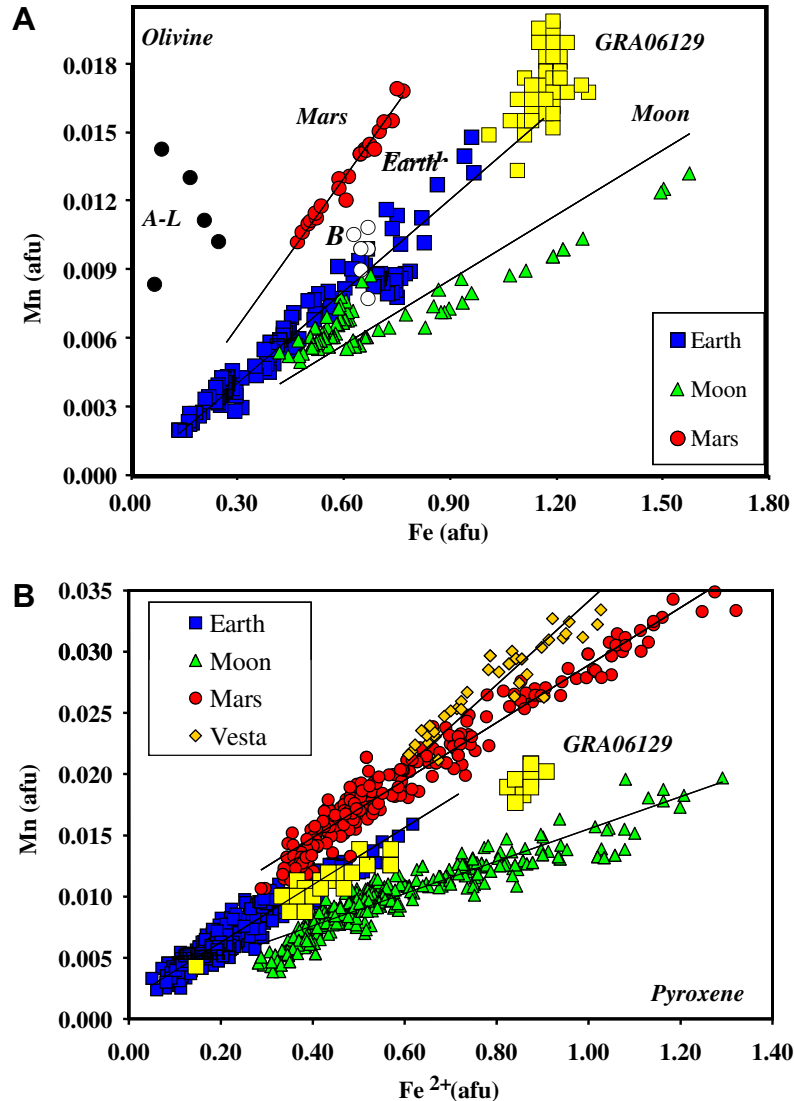
Fig. 16. Fe (atoms per formula unit) vs Mn (atoms per formula unit) for olivine and pyroxene for GRA (yellow squares) and other planetary bodies. B, brachinites (open circles), A and L, acapulcoites and lodranites (black circles). Data for terrestrial basalts (blue squares), lunar basalts (green triangles), and martian basalts (red circles) are from Karner et al. (2003, 2006).

primitive achondrites commonly represent mixtures of residuum and the first partial melts of a chondritic source reservoir. Although not all potential compositions that could be extracted from chondritic precursors have been identified in the meteorite collection, both achondrite meteorite observations and chondrite melting experiments indicate that melt compositions ranging from initial low-temperature (950–980°) Fe–Ni sulfide melts to basalts (at higher-temperature, i.e., >1050 °C) can be produced during episodes of asteroidal melting (Jurewicz et al., 1991; Nehru et al., 1992, 1996; Jones et al., 1994; McCoy et al., 1997; Benedix et al., 1998; Mittlefehldt et al., 1998; Floss, 2000). Several studies have predicted that at intermediate temperatures (between sulfide melts and basaltic melts) more sodic partial melts may be produced from a chondrite source (Floss, 2000; Feldstein et al., 2001; Ikeda and Prinz, 2001; Cohen et al., 2004; Kita et al., 2004; Goodrich et al.,

2007). The GRA meteorites appear represent the crystallization product of such a relatively unique melt produced during melting at these intermediate conditions.

Although the mineral assemblage in GRA is rare in the meteorite collection, unusual occurrences of similar assemblages have been identified in some meteorites. Minute, relatively rare clasts and inclusions containing sodic feldspar have been identified in chondrites and ureilites such as Kaidun, Adzhi-Bogdo, and Dar al Gani 319 (Ikeda and Prinz, 2001). The inclusions contain glass with high Na_2O (up to 7.4 wt.%), whereas mesostasis associated with felsic lithic clasts can contain up to 11% Na_2O. Sodic plagioclase compositions ranging from An_{2-21} have been identified by Ikeda and Prinz (2001), Kita et al. (2004) and Cohen et al. (2004). The inclusions and sodic feldspar assemblages in polymict ureilites have been studied in further detail by Kita et al. (2004) and Cohen et al. (2004). These studies suggested potential

origins for these assemblages and, along with Goodrich et al. (2007), placed them within the context of melting on the ureilite parent body. Sodic plagioclase ($An_{25-7.7}$) has been identified in winonaites (Benedix et al., 1998) in pyroxene-plagioclase "melt pockets". Takeda et al. (2001) described both inclusions and segregations with sodic feldspar compositions in a variety of iron meteorites (IAB, IA, IIE) that are similar to those in winonaites (e.g., the average plagioclase in clasts in Campo del Cielo is $Or_{2.8} Ab_{84.2} An_{13}$). Furthermore, Takeda et al. (2001) showed that some of these melts approached an "andesite" bulk composition.

Clearly, many of these observations indicate that melts capable of producing GRA-type mineral assemblages can be generated by melting of chondritic material on numerous parent bodies. Benedix et al. (1998) proposed that the silicate melts in winonaites (sodic plagioclase–calcic pyroxene segregations) were produced at approximately 1050 °C and followed the production and partial remobilization of Fe, FeS–Ni eutectic melts. Further, they concluded that these "melt pockets" were produced through the melting of a heterogeneous chondritic precursor with a composition unlike those of any chondrites represented in the current meteorite collection. In iron meteorites, Takeda et al. (2001) called upon the production and segregation of Fe–Ni–S–P eutectic melt and Ca-, Al-, Na-rich silicate partial melt adjacent to chondritic source material (prior to catastrophic mixing of silicates and metals). Ikeda and Prinz (2001), Cohen et al. (2004) and Kita et al. (2004) suggested that the Na-feldspar-rich lithologies represent melts that were produced by small degrees (<10%) of fractional melting of the ureilite parent body (UPB) with a composition similar to an alkali-rich carbonaceous chondrite. Can such low melt fractions be physically extracted from source regions on a small planetary body such as the UPB or the GRA parent body?

Within the context of physical models for the extraction and transport of small melt fractions on the UPB, Goodrich et al. (2007) suggested that these melts would be capable of migrating out of their source region after only 1–2% melting and would migrate continuously (disequilibrium fractional melting) and rapidly (on a time scale of years) in a network of veins and dikes. The production of CO and CO_2 gas by smelting over the course of melting on the UPB (Goodrich et al., 2007) would have enhanced the migration capability of these small melt fractions. The smelting process would have occurred under much more reducing conditions (more reducing than IW) than suggested by our estimates of f_{O2} for GRA (>IW). Therefore, CO and CO_2 gas enabled migration of melts on the GRA parent body appears unlikely. However, migration capability may have been enhanced through the availability of other volatiles such as water. Boudreau et al. (1997) and Patiño Douce and Roden (2006) suggested that high Cl/F in apatite reflects the enrichment of other volatile elements such as water. The Q-Xenon is typical of primitive chondritic meteorites and its presence here demonstrates retention of a significant signature of extreme volatiles from a presumed primitive parent.

Although numerous geochemical fingerprints indicate GRA is not derived from the parent bodies of the ureilites

or winonaites (i.e., GRA has higher Fe/Mn in pyroxene and olivine, lower CaO in olivine, and significantly different O isotopic signatures), the processes proposed for the generation of the Na-rich feldspar lithologies observed in these achondrites are probably highly relevant to the petrogenesis of GRA. Over the last few decades, numerous chondrite melting experiments (e.g., Kushiro and Mysen, 1979; Takahashi, 1983; Jones et al., 1994; Jurewicz et al., 1991) have demonstrated that both low temperature Fe–S–Ni melts and higher temperature basaltic melts can be generated through equilibrium melting. Jones et al. (1994) showed that non-cumulate eucrites may be produced in this manner. These experimental studies and other computational approaches do not replicate the disequilibrium melting processes invoked by Ikeda and Prinz (2001), Goodrich et al. (2007) and Kita et al. (2004). Disequilibrium melting experiments of an L6 chondrite conducted by Feldstein et al. (2001) offer a unique perspective into these types of melting processes. They observed that small degrees of melting (10–15%) of a L6 chondrite (Na_2O ~0.95 wt.%) would produce pockets of melt with high-Na and high normative-plagioclase. These pockets appear to be closely associated with the localized melting of plagioclase and phosphates. Fig. 17 illustrates the similarity of the REE patterns of one of these melt pockets and the GRA whole rock. Also, shown for comparison are the REE patterns of an L6 chondrite and a residuum calculated after the removal of a Na-rich melt. The calculated residuum is slightly more depleted in REE and LREE than brachinite ALH 84025, but is significantly different from the generally LREE enriched brachinites represented by Eagles Nest and Brachina (Mittlefehldt et al., 1998). As shown it Fig. 17, small degrees of partial melting of a chondritic source would produce a melt that is enriched in $(Na/Sc)_{CI}$ and $(Sm/Sc)_{CI}$ similar to GRA and produce a residuum that is depleted in both $(Na/Sc)_{CI}$ and $(Sm/Sc)_{CI}$ similar to the ALH 84025 brachinite, ureilites, and lodranites. The winonaites, acapulcoites, and several of the other brachinites that plot near the $(Na/Sc)_{CI}$ and $(Sm/Sc)_{CI}$ values of 1 experienced melting but less efficient silicate melt removal (McCoy et al., 1997; Mittlefehldt et al., 1998).

Kita et al. (2004) modeled the behavior of K, Ba, and Sr during both equilibrium and fractional melting of CI and CM chondrites as a means of evaluating the role of melting in the petrogenesis of the sodic-rich lithologies in ureilites (Fig. 18). In addition to their partial melting models, we also modeled equilibrium and fractional melting of an L chondrite bulk composition that was similar to that experimentally studied by Feldstein et al. (2001). These melting models are compared to bulk GRA and glass compositions from the work of Feldstein et al. (2001) in Fig. 18. Based on the models for melting of CI and CM chondrites, Kita et al. (2004) concluded that small degrees of fractional melting were important in producing the sodic-feldspar rich assemblages in ureilites. Within the context of these models for the behavior of K, Ba, and Sr, GRA appears to be derived from the crystallization of a melt that was produced by 10% fractional melting of an L chondrite parent body.

The enrichment of these low-fraction melting products in both Na and normative plagioclase can be further
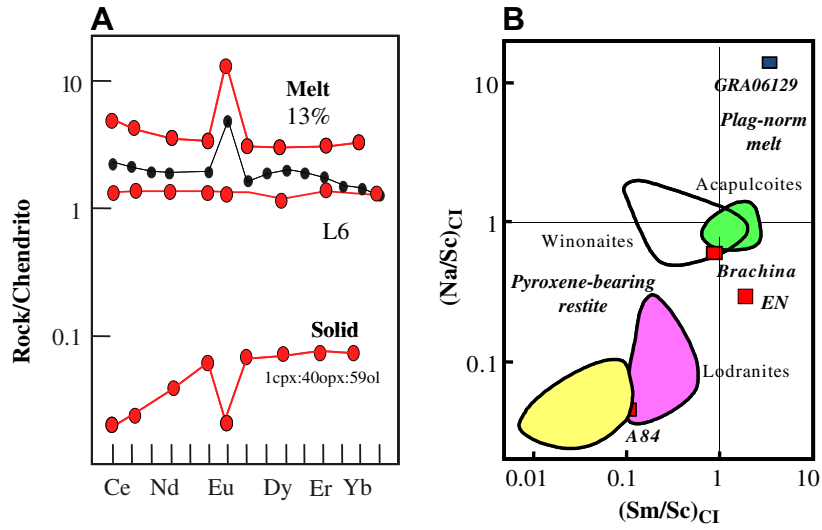
Fig. 17. (A) Plot of REE for GRA (black data points) compared to REE patterns for an L6 chondrite, a melt pocket produced during melting (13%) of an L6 chondrite as determined by Feldstein et al. (2001), and a calculated residuum resulting from the extraction of the Feldstein et al. (2001) produced melt from an L6 chondrite (three patterns shown in red). (B) Plot of Na/Sc vs Sm/Sc for bulk GRA 06129. This is compared to fields defined for winonaites, acapulcoites, urelites, lodranites, and brachinites (points Brachina, EN, A84). Melting (batch or fractional) of a parent body with (Na/Sc)$_{CI}$ and (Sm/Sc)$_{CI}$ = 1 will yield a melt in the plag (plagioclase)-norm melt field and a residuum in the pyroxene-bearing restite field.
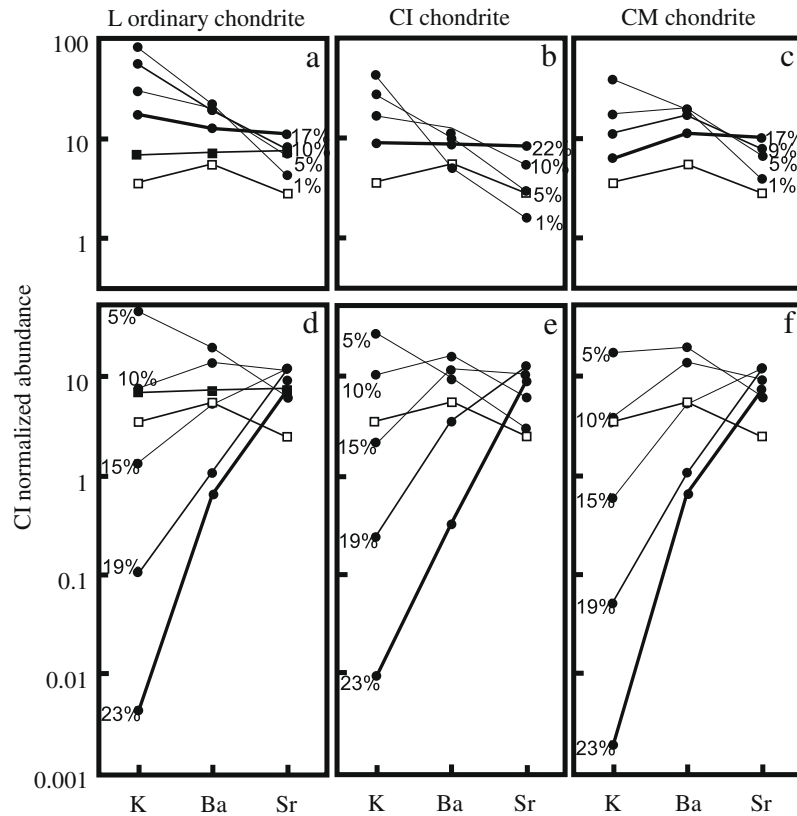

Fig. 18. Trace element abundances of melts during partial melting of chondritic precursors (L ordinary chondrite, CI chondrite, and CM chondrite). Figures a, b, and c are batch melting models for K, Ba, and Sr. Figures d, e, f are 5% fractional melting models with repeated melt extraction with increased melting. Superimposed on all figures are the values for GRA from Table 2 (open squares) and data from melt pockets from the experimental study of Feldstein et al. (2001) (filled squares in L chondrite model). Modified after Kita et al. (2004).
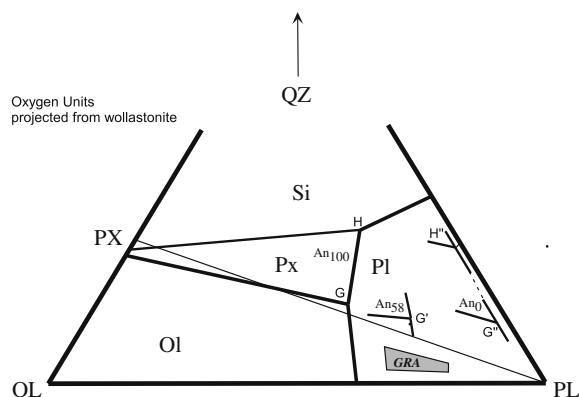
Fig. 19. Olivine–plagioclase–quartz system projected from wollastonite (in oxygen units). Superimposed on this system are isopleths of the Fo–En and En–Pl cotectic surfaces and pertectic (G, G′, G″) and cotectic (H, H‴) reaction points are from Sessler et al. (1982) with decreasing An/(An + Ab). This illustrates that melting of a Na-rich chondrite will yield a melt with high normative abundances of plagioclase and more sodic normative plagioclase.

influenced by the bulk composition of the precursor chondrite material. In the forsterite–anorthite–SiO_2 system, the first melt is at the peritectic (reaction point G in Fig. 19) and contains approximately 55% plagioclase. Sessler et al. (1982) demonstrated that within the forsterite–plagioclase–SiO_2 system, an increase in the sodium content of the precursor chondrite causes reaction points G (plagioclase + pyroxene ⇔ olivine + melt G) and H (plagioclase + pyroxene + SiO2 ⇔ melt H) to move toward the plagioclase–SiO_2 join (Fig. 19). Initial melting of an alkali-rich chondrite will produce a melt at a reaction point between points G′ and G″ until the plagioclase component is consumed leaving a residuum of olivine and pyroxene. This is the rationale behind the requirement of an alkali-rich chondrite source for the models proposed by Ikeda and Prinz (2001) and Kita et al. (2004) for melting on the UPB. Alternatively, Arai et al. (2008) suggested that melting of a volatile-rich, chondrite parent body may produce "andesite" melts that are rich in normative sodic plagioclase.

The earliest melt produced from an ordinary chondrite protolith forms at the Fe, Ni–FeS eutectic at approximately 950 °C. The effect of this melting and melt extraction is clearly seen in primitive achondrites such as the acapulcoites and lodranites. There is some petrologic and geochemical evidence for the melting and extraction of this low temperature melt prior to the generation of the silicate melt from the asteroid source of GRA. The low [chalcophile element/Sc]$_{CI}$ ratio of the bulk GRA probably reflects the production and segregation of a low temperature sulfide melt from the GRA source. This Fe–Ni–S melt was only partially removed and a portion was mixed with the higher temperature silicate melt. Our interpretation of the two sulfide–metal inclusions in the olivine in GRA is that they represent a remnant of the low temperature sulfide melt. An approximation of the composition of this melt and its post-entrapment crystallization history is partially reconstructed in Fig. 8.

It is important to emphasize that GRA itself does not represent a melt composition, but most likely represents the accumulation of plagioclase from such a melt. There are numerous lines of evidence to support its origin as a cumulate. First, the high modal abundance of plagioclase (at least 80% plagioclase) and the positive Eu anomaly observed in the REE pattern for the bulk GRA suggest the accumulation of plagioclase. Second, there is no textural evidence that this rock represents a melt. To the contrary, textures are like those preserved in plagioclase-rich planetary cumulates such as the cumulate eucrites and lunar ferroan anorthosites. Finally, the bulk composition of GRA is offset from reaction points G, G′, and G″ (Fig. 19) making it less likely (although not impossible) to represent a melt. Accumulation of plagioclase during magmatic processes on a small asteroid is possible as illustrated by the cumulate eucrites that presumably were formed on asteroid 4 Vesta.

As an alternative to formation from low degrees of partial melting, it has been proposed that GRA could represent an asteroidal crust produced by plagioclase accumulation either during global planetary differentiation (i.e., magma ocean) (Zeigler et al., 2008) or crystallization of a large magma body (i.e., layered intrusion). Indeed, the magnetic properties of GRA suggests the possibility that the GRA parent body may have been large enough to have generated an internal magnetic field, which could indicate high enough degrees of planetary melting to have led to the formation of a metallic core. The global differentiation model would be analogous to the lunar ferroan anorthosites that were produced during the initial stages of differentiation by plagioclase flotation in a magma ocean (e.g., Shearer et al., 2006, and references within). Although planetary bodies the size of the Moon are more likely to have primary plagioclase crust during planetary differentiation (due to pressure regimes under which a magma ocean would have crystallized), spectral analysis of >100 asteroids does not hint at a crust dominated by plagioclase (Bell et al., 1989). Even more damaging to this hypothesis is that on very small bodies (i.e., asteroids), it is difficult to separate pyroxene from plagioclase during the crystallization of a magma ocean (Taylor et al., 1993). For example, differentiated asteroid 4 Vesta, which is thought to have experienced differentiation via a magma ocean (Righter and Drake, 1997), contains a basaltic crust and not a plagioclase-rich crust. It is also unlikely that a layered intrusion from an asteroid would produce a late-stage lithology that is as depleted in incompatible elements as GRA. Plagioclase-enriched cumulates produced via crystallization of asteroidal basalts (cumulate eucrites) have similar REE patterns as GRA, but have significantly more calcic plagioclase ($An_{93}Ab_6Or_{0.5}$ to $An_{72}Ab_{26}Or_2$). Therefore, the most plausible mechanism to produce GRA is through small degrees of partial melting of a chondritic parent body followed by accumulation of plagioclase and phosphates.

The difference in early solar system magmatism represented by GRA compared to the eucrites and angrites is tied to parent body composition and the early thermal history of that body. The HED and angrite parent bodies accreted with low concentrations of moderately-volatile elements, whereas the GRA parent body accreted with

chondritic abundances of moderately-volatile elements. The GRA parent body also experienced substantially lower degrees of melting than the eucrite and angrite parent body.

4.5. Post-magmatic crystallization processes

There is textural and chemical evidence for at least four episodes of post-magmatic crystallization processes: (1) Subsolidus reequilibration of silicates, oxides, and sulfides, (2) Formation of granoblastic textures due to impact events, (3) Late-stage Cl alteration of pyroxene and merrillite, and (4) Low-temperature alteration along grain boundaries and within fractures.

Processes 1 and 2 have been briefly discussed within the context of cation exchange among phases, exsolution phenomena associated with pyroxene and sulfides, and the granoblastic texture exhibited by GRA. Geothermometry suggests that these feature are developed between 962 and 600 °C.

The late-stage replacement of pyroxene and merrillite by chloroapatite may be the result of either near-subsolidus interaction between these magmatic phases and a high-T chlorine-rich residuum melt/fluid or a lower temperature interaction with a chlorine-rich fluid. In the case of the former, the melt/fluid is magmatic in origin and may reflect similar processes as called upon for Cl enrichments in portions of the Bushveld and Stillwater complexes on Earth (Willmore et al., 2000). In the case of the latter, the lower temperature Cl-rich fluid may be magmatic in origin or derived from other parent body sources. While there is little evidence to distinguish between these models for the origin of the Cl-replacement, textural observations may be interpreted as indicating merrillite was partially protected from Cl alteration adjacent to olivine grain boundaries. Most of these merrillite–olivine grain boundaries were formed during the formation of the granoblastic texture.

The megascopic view of the GRA meteorites indicates that they have undergone significant low-temperature alteration. The microscopic view indicates that this alteration is pervasive adjacent to mineral surfaces and in fractures in mineral grains. Initial observations indicate that there are at least three types of low-temperature alteration in this meteorite: alteration that primarily consists of Fe-bearing phases, alteration that consists of Fe-rich phases, sulfates and perhaps sulfides, and alteration of olivine to "iddingsite". Zeigler et al. (2008) tentatively identified gypsum and bassanite of seemingly terrestrial origin near the exterior of the meteorites. Magnetic properties of a bulk sample of GRA06129 suggest that one of the high coercivity magnetic phases is hematite. However, FTIR measurements do not identify hematite or goethite as a phase in the alteration. Rather, they suggest that the Fe occurs in an amorphous admixture. It is unclear if this extensive alteration preserves a low-temperature parent body process or if it is simply terrestrial. If the former, it is also uncertain how much of the alteration has been modified by interactions with terrestrial fluids.

Several observations that were made on the low-temperature alteration in GRA meteorites that hint at a low-temperature parent body component that may have been disturbed by terrestrial alteration. The meteorite contains abundant low-temperature phases, yet the fusion crust appears to be glassy with very minor alteration. There appears to be a spatial relationship between the distribution of the different types of alteration mineralogies and the fusion crust. Yet, some stages of alteration occur in veins that cross-cut the fusion crust and appear to replace partially melted olivine adjacent to the fusion crust (Fig. 4C).

Pyroxenes and feldspars have both been demonstrated to be retentive iodine carriers (Brazzle et al., 1999; Gilmour et al., 2000). However, the distribution among our three samples and the observation that a single step in the analysis of 231 contributed 70% of the iodogenic ^{129}Xe in this sample suggests a contribution from a minor phase, perhaps halogen-rich apatite or alteration products. These data suggest that there is no evidence of a significant contribution of xenon from the terrestrial atmosphere as might be expected from significant terrestrial weathering.

The low temperature release pattern for hydrogen and carbon and thermal demagnetization are consistent with the breakdown of a ferric hydroxide between 100 and 200 °C. Although the FTIR measurements indicate that the ferric hydroxide component is most likely in an amorphous admixture and/or perhaps Fe^{3+}–O–H and not goethite, if we assume that the 1000 ln δD value for most ferric hydroxides–water is similar to goethite–water ($\sim -110‰$ at 25 °C) and is temperature insensitive (Yapp and Pedley, 1985), the water in equilibrium with the sample should have δD values close to 0‰. If the meteorite had hydrated in equilibrium with the Antarctic ice (δD value of -350 to $-400‰$), then the δD values should be extremely light. The relatively high δD values measured in this sample strongly support a component in the alteration that represents an extraterrestrial origin for hydration.

Finally, the average $\delta^{13}C$ value for GRA 06129 is $-25.5‰$ (PDB), and corresponds with the field of values measured for acid residues in carbonaceous chondrites (Krouse and Modzeleski, 1970). It also coincides with the average $\delta^{13}C$ value for terrestrial goethite (Yapp and Poths, 1986). The origin of the carbon is ambiguous on the basis of the carbon isotope value alone, but given that the δD values could not have been acquired by equilibrium with Antarctic ice, it is reasonable to assume that the carbon is also of extraterrestrial origin.

5. CONCLUSIONS

The GRA achondrites provide a unique perspective of planetesimal processes during the earliest stages of solar system history that is rarely represented in the meteorite collection. First, the very earliest stages of planetesimal melting that were likely driven by the decay of short-lived radionuclides do not necessarily yield basaltic melts. This is contrary to the commonly held view that the earliest stages of melting on all planetary bodies during the first 2–30 million years of solar system history were fundamentally basaltic in nature. The fundamental difference between magmatism represented by GRA and magmatism represented by the eucrites and angrites is tied to parent body composition and thermal history. Whereas, eucrites and angrites represent extensive melting of

a parent body with low concentrations of moderately-volatile elements, GRA represents low-degrees of melting of a parent body with chondritic abundances of moderately volatile elements. Although poorly represented in the meteorite collection, there is no reason to believe that this is a rare asteroidal process in the early solar system. Second, GRA represents a series of early asteroidal processes: (stage 1) Melting and partial extraction of a low-temperature Fe–Ni–S melt; (stage 2) Small degrees of disequilibrium partial melting of a sodium- or alkali-rich chondritic parent body with additional incorporation of Fe–Ni–S melt that was not fully extracted during stage 1; (stage 3) Rapid extraction and emplacement of the Na-rich, high-normative plagioclase melt similar to models proposed by Goodrich et al. (2007). However, unlike the model proposed by Goodrich et al. (2007), extraction was enhanced by volatiles such as H_2O rather than $CO–CO_2$; (stage 4) Final emplacement and accumulation of plagioclase and phosphates, (stage 5) Subsolidus reequilibration of the lithology between 962 and 600 °C; and (stage 6) Replacement of merrillite and pyroxene by Cl-apatite resulting from the interaction between magmatic minerals and a Cl-rich residuum melt/fluid. The interpretation of the low-temperature alteration assemblage dominated by amorphous admixture and Cl-, S-bearing phases is somewhat ambiguous. Textural features suggest multiple episodes of alteration. The last episode of alteration appears to cross-cut the fusion crust and earlier stages of alteration. This stage is clearly of terrestrial origin. Xenon and stable isotopic measurements of the alteration may be interpreted as indicating an extraterrestrial volatile component was preserved in GRA. If this is true, it implies that on the GRA parent body either a volatile reservoir survived the melting event on a relatively small parent body, a fluid phase existed following the magmatic crystallization of GRA, or that a late-stage volatile component was added to the parent body following parent body melting and metamorphism.

ACKNOWLEDGMENTS

APPENDIX A. SUPPLEMENTARY DATA

Supplementary data associated with this article can be found, in the online version, at doi:10.1016/j.gca.2009.10.029.

REFERENCES

Amelin Y. (2008a) U–Pb ages of angrites. *Geochim. Cosmochim. Acta* **72**, 221–232.

Amelin Y. (2008b) The U–Pb systematics of angrite Sahara 99555. *Geochim. Cosmochim. Acta* **72**, 4874–4885.

Amelin Y. and Pravdivtseva O. (2005) U–Pb age of the acapulco phosphate: testing the calibration of the I–Xe chronometer. *Meteorit. Planet. Sci.* **40**, A5106.

Amelin Y., Krot A. N., Hutcheon I. D. and Ulyanov A. A. (2002) Lead isotopic ages of chondrules and calcium–aluminum-rich inclusions. *Science* **297**, 1678–1683.

Anders E. and Grevesse N. (1989) Abundances of the elements: meteoritic and solar. *Geochim. Cosmochim. Acta* **53**, 197–214.

Arai T., Tomiyama T., Saiki K. and Takeda H. (2008) Unique achondrite GRA 06128/06129: andesitic partial melt from a volatile-rich parent body. *Lunar and Planetary Science XXXIX*, Lunar Planetary Institute, Houston. #2465 (abstr.).

Ash R. D., Day J. M. D., McDonough W. F., Bellucci J., Rumble D., Liu Y., and Taylor L.A. (2008) Petrogenesis of the differentiated achondrite GRA 06129: trace elements and chronology. *Lunar and Planetary Science XXXIX*. Lunar Planetary Institute, Houston. #2271 (abstr.).

Balacescu A. and Wänke H. (1977) $^{40}Ar/^{39}Ar$ ages of achondrites. *Meteoritics* **29**, 439–440.

Bell J. F., Davis D. R., Hartmann W. K. and Gaffey M. J. (1989) Asteroids: the big picture. In *Asteroids II* (eds. R. P. Binzel, T. Gehrels and M. S. Matthews). University of Arizona Press, Tucson, Arizona, p. 921–945.

Benedix G. K., McCoy T. J. and Keil K. (1998) A petrologic and isotopic study of winonaites: evidence for early partial melting brecciation, and metamorphism. *Geochim. Cosmochim. Acta* **62**, 2535–2553.

Bogard D. D. (1995) Impact ages of meteorites: a synthesis. *Meteoritics* **30**, 244–268.

Boudreau A. E., Stewart M. A. and Spivack A. J. (1997) Stable chlorine isotopes and the origin of high-Cl magmas of the stillwater complex, Montana. *Geology* **25**, 791–794.

Bouvier A. and Wadhwa M. (2009) Synchronizing the absolute and relative clocks: Pb–Pb and Al–Mg systematics in CAIs from the Allende and NWA 2364 CV3 chondrites. *Lunar and Planetary Science XL*. Lunar Planetary Institute, Houston. #2184 (abstr.).

Brazzle R. H., Pravdivtseva O. V., Meshik A. P. and Hohenberg C. M. (1999) Verification and interpretation of the I–Xe chronometer. *Geochim. Cosmochim. Acta* **63**, 739–760.

Burkhardt C., Kleine T., Bernard B., Palme H., Zipfel J., Friedrich J. M. and Ebel D. S. (2008) Hf-W mineral isochron for Ca, Al-rich inclusions: age of the Solar System and the timing of core formation in planetesimals. *Geochim. Cosmochim. Acta* **72**, 6177–6197.

Busemann H., Baur H. and Wieler R. (2000) Primordial noble gases in "Phase q" in carbonaceous and ordinary chondrites studied by closed-system stepped etching. *Meteorit. Planet. Sci.* **35**, 949–973.

Busfield A., Turner G. and Gilmour J. D. (2008) Testing an integrated chronology: I–Xe analysis of enstatite meteorites and a eucrite. *Meteorit. Planet. Sci.* **43**, 883–897.

Catanzaro E., Murphy T., Garner E. and Shields W. (1966) Absolute isotopic abundance ratios and atomic weight of magnesium. *J. Res. Nat. Bureau Stand.* **70A**, 456–458.

Cisowski S. (1981) Interacting vs. non-interacting single domain behavior in natural and synthetic samples. *Phys. Earth Planet. Int.* **26**, 56–62.

Clayton R. N. and Mayeda T. K. (1996) Oxygen isotope studies of achondrites. *Geochim. Cosmochim. Acta* **60**, 1999–2017.

Cohen B. A., Goodrich C. A. and Keil K. (2004) Feldspathic clast populations in polymict ureilites: stalking the missing basalts from the ureilite parent body. *Geochim. Cosmochim. Acta* **68**, 4249–4266.

Connelly J. N., Amelin Y., Krot A. N. and Bizzarro M. (2008) Chronology of the Solar System's oldest solids. *Astrophys. J.* **675**, L121–L124.

Crowther S. A., Mohapatra R. K., Turner G., Blagburn D. J., Kehm K. and Gilmour J. D. (2008) Characteristics and applications of RELAX, an ultrasensitive resonance ionization mass spectrometer for xenon. *J. Anal. Atomic Spectrom.* **23**, 938–947.

Crowther S. A., Whitby J. A., Busfield A., Holland G., Busemann H. and Gilmour J. D. (2009) Collisional modification of the acapulcoite/lodranite parent body revealed by the iodine–xenon system in lodranites. Meteorit. Planet. Sci., in press.

Day J. M. D., Ash R. D., Liu Y., Bellucci J. J., Rumble D., McDonough W. F., Walker R. J. and Taylor L. A. (2009) Early formation of evolved asteroidal crust. *Nature* **457**, 179–183.

Droop G. T. R. (1987) A general equation for estimating Fe^{3+} in ferromagnesian silicates and oxides from microprobe analyses, using stoichiometric criteria. *Mineral. Mag.* **51**, 431–435.

El-Hinnawi E. E. (1966) *Methods in Chemical and Mineral Microscopy*. Elsevier Publishing Company, New York, New York, 222p..

Feldstein S. N., Jones R. H. and Papike J. J. (2001) Disequilibrium partial melting experiments on the Leedey L6 chondrite: textural controls on melting processes. *Meteorit. Planet. Sci.* **36**, 1421–1441.

Fernandes V. A., Burgess R., Bischoff A. and Metzler K. (2006) Ar composition of the melt lithology within the NWA 2457 breccia. *Meteorit. Planet. Sci.* **41**, A5308.

Floss C. (2000) Complexities in the acapulcoites–lodranite parent body: evidence from trace element distributions in silicate minerals. *Meteorit. Planet. Sci.* **35**, 1073–1085.

Ghiorso M. S. and Sack R. O. (1991) Fe–Ti oxide geothermometry–thermodynamic formulation and the estimation of intensive variables in silicic magmas. *Contrib. Mineral. Petrol.* **108**(4), 485–510.

Giesemann A., Jaeger H. J., Norman A. L., Krouse H. R. and Brand W. A. (1994) On-line sulfur-isotope determination using an elemental analyzer coupled to a mass spectrometer. *Anal. Chem.* **66**, 2816–2819.

Gilmour J. D., Lyon I. C., Johnston W. A. and Turner G. (1994) RELAX – an ultrasensitive, resonance ionization mass-spectrometer for xenon. *Rev. Sci. Instrum.* **65**, 617–625.

Gilmour J. D., Whitby J. A., Turner G., Bridges J. C. and Hutchison R. (2000) The iodine–xenon system in clasts and chondrules from ordinary chondrites: implications for early solar system chronology. *Meteorit. Planet. Sci.* **35**, 445–456.

Glavin D. P., Kubny A., Jagoutz E. and Lugmair G. W. (2004) Mn–Cr isotope systematic of the D'Orbigny angrite. *Meteorit. Planet. Sci.* **39**, 693–700.

Goodrich C. A., Herd C. D. K. and Taylor L. A. (2003) Spinels and oxygen fugacity in olivine-phyric and lherzolitic shergottites. *Meteorit. Planet. Sci.* **38**(12), 1773–1792.

Goodrich C. A., Van Orman J. A. and Wilson L. (2007) Fractional melting and smelting on the ureilite parent body. *Geochim. Cosmochim. Acta* **71**, 2876–2895.

Herd C. D. K. (2008) Basalts as probes of planetary interior redox state. *Rev. Mineral. Geochem.* **68**, 527–553.

Herd C. D. K., Borg L. E., Jones J. H. and Papike J. J. (2002) Oxygen fugacity and geochemical variations in the martian basalts: implications for martian basalt petrogenesis and the oxidation state of the upper mantle of Mars. *Geochim. Cosmochim. Acta* **66**(11), 2025–2036.

Hsieh K. C., Vlach K. C. and Chang Y. A. (1987) The Fe–Ni–S system I. A thermodynamic analysis of the phase equilibria and calculation of the phase diagram from 1173 to 1623 K: high Temperature. *Science* **23**, 17–37.

Ikeda Y. and Prinz M. (2001) Magmatic inclusions and felsic clasts in the Dar al Gani 319 polymict ureilite. *Meteorit. Planet. Sci.* **36**, 481–499.

Jacobsen B., Yin Q. Z., Moynier F., Amelin Y., Krot A. N., Nagashima K., Hutcheon I. D. and Palme H. (2008) ^{26}Al–^{26}Mg and ^{207}Pb–^{206}Pb systematics of Allende CAIs: canonical solar initial $^{26}Al/^{27}Al$ ratio reinstated. *Earth Planet. Sci. Lett.* **272**, 353–364.

Jones J. H., Jurewicz A. J. G. and Mittlefehldt D. W. (1994) The compositional similarity between Sioux County and experimentally-produced partial melts of the Murchison chondrite favors a partial melting origin for primitive eucrites. *Lunar Planet. Sci.* **25**, 639–640.

Jourdan F., Verati C. and Féraud G. (2006) Intercalibration of the Hb3gr $^{40}Ar/^{39}Ar$ dating standard. *Chem. Geol.* **231**, 177–189.

Jurewicz A. J. G., Mittlefehldt D. W. and Jones J. H. (1991) Partial melting of the Allende (CV) meteorite: implications for the origins of basaltic meteorites. *Science* **252**, 695–698.

Karner J. M., Papike J. J. and Shearer C. K. (2003) Olivine from planetary basalts: chemical signatures that indicate planetary parentage and those that record igneous settings and process. *Am. Mineral.* **88**, 806–816.

Karner J. M., Papike J. J. and Shearer C. K. (2006) Comparative planetary mineralogy: Pyroxene major- and minor-element chemistry and partitioning of vanadium between pyroxene and melt in planetary basalts. *Am. Mineral.* **91**, 1574–1582.

Kita N. T., Ikeda Y., Togashi S., Liu Y., Morishita Y. and Weisberg M. K. (2004) Origin of ureilites from a SIMS oxygen isotopic and trace element study of clasts in the Dar al Gani 319 polymict ureilite. *Geochim. Cosmochim. Acta* **68**, 4213–4235.

Kleine T., Mezger K., Palme H., Scherer E. and Münker C. (2005) Early core formation in asteroids and late accretion of chondrite parent bodies: evidence from ^{182}Hf–^{182}W in CAIs, metal-rich chondrites, and iron meteorites. *Geochim. Cosmochim. Acta* **69**, 5805–5818.

Krouse H. R. and Modzeleski V. E. (1970) C13/C12 abundances in components of carbonaceous chondrites and terrestrial samples. *Geochim. Cosmochim. Acta* **34**, 459–474.

Kusakabe M., Maruyama S., Nakamura T. and T.Y. (2004) CO_2 Laser-BrF5 fluorination technique for analysis of oxygen three isotopes of rocks and minerals. *J. Mass Spectrom. Soc. Jpn.* **52**, 205–212.

Kushiro I. and Mysen B. O. (1979) Melting experiments on a Yamato chondrite. *Memoirs Natl. Inst. Polar Res.* **15**, 165–170 (special issue).

Lindsley D. H. (1983) Pyroxene thermometry. *Am. Mineral.* **68**, 477–493.

Lowrie W. (1990) Identification of ferromagnetic minerals in a rock by coercivity and unblocking temperature properties. *Geophys. Res. Lett.* **17**, 159–162.

Lugmair G. W. and Shykolyukov A. (1998) Early solar system timescales according to ^{53}Mn–^{53}Cr systematics. *Geochim. Cosmochim. Acta* **62**, 2863–2886.

Markowski A., Quitté G., Kleine T., Halliday A. N., Bizzarro M. and Irving T. (2007) Hafnium tungsten chronometry of angrites and the earliest evolution of planetary objects. *Earth Planet. Sci. Lett.* **262**, 214–229.

Markowski A., Quitté G., Halliday A. N. and Kleine T. (2006) Tungsten isotopic compositions of iron meteorites: Chronological constraints vs. cosmogenic effects. *Earth Planet. Sci. Lett.* **242**, 1–15.

McCoy T. J., Keil K., Muenow D. W. and Wilson L. (1997) Partial melting and melt migration in the acapulcoite–lodranite parent body. *Geochim. Cosmochim. Acta* **61**, 639–650.

McKay G., Le L., Wagstaff J. and Crozaz G. (1994) Experimental partitioning of rare earth elements and strontium: Constraints on petrogenesis and redox conditions during crystallization of Antarctic angrite Lewis Cliff 86010. *Geochim. Cosmochim. Acta* **58**, 2911–2919.

Mittlefehldt D. W., McCoy T. J., Goodrich C. A. and Kracher A. (1998) Non-chondritic meteorites from asteroidal bodies. In *Planetary Materials, vol. 36* (ed. J. J. Papike). Mineralogical Society of America, Chantilly, Virginia, pp. 4–1 to 4–195.

Moskowitz B. M., Frankel R. B. and Bazylinski D. A. (1993) Rock magnetic criteria for the detection of biogenic magnetite. *Earth Planet. Sci. Lett.* **120**, 283–300.

Neal C. R. (2001) The interior of the Moon: the presence of garnet in the primitive, deep lunar mantle. *J. Geophys. Res.* **106**, 27865–27885.

Nehru C. E., Prinz M., Weisberg M. K., Ebihara M. E., Clayton R. N. and Mayeda T. K. (1992) Brachinites: a new primitive achondrite group. *Meteoritics* **27**, 267.

Nehru C. E., Prinz M., Weisberg M. K., Ebihara M. E., Clayton R. N. and Mayeda T. K. (1996) A new brachinite and petrogenesis of the group. *Lunar Planet. Sci.* **27**, 943–944.

Nichols, Jr., R. H., Hohenberg C. M., Kehm K., Kim Y. and Marti K. (1994) I–Xe studies of the acapulco meteorite: absolute I–Xe ages of individual phosphate grains and the Bjurböle standard. *Geochim. Cosmochim. Acta* **58**, 2553–2561.

Niemeyer S. (1980) I–Xe and $^{40}Ar/^{39}Ar$ analyses of silicate from Weekeroo Station and Netschaëvo IIE iron meteorites. *Geochim. Cosmochim. Acta* **44**, 1829–1840.

Nyquist L. E., Reese Y., Wiesmann H., Shih C. Y. and Takeda H. (2003) Fossil ^{26}Al and ^{53}Mn in the Asuka 881394 eucrite: Evidence of the earliest crust on asteroid 4 Vesta. *Earth Planet. Sci. Lett.* **214**, 11–25.

Patiño Douce A. E. and Roden M. (2006) Apatite as a probe of halogen and water fugacities in the terrestrial planets. *Geochim. Cosmochim. Acta* **70**, 3173–3196.

Patzer A., Schultz L. and Franke L. (2003) New noble gas data of primitive and differentiated achondrites including Northwest Africa 011 and Tafassasset. *Meteorit. Planet. Sci.* **38**, 1485–1497.

Pellas P., Fieni C., Trieloff M. and Jessberger E. K. (1997) The cooling history of the Acapulco meteorite as recorded by the ^{244}Pu and ^{40}Ar–^{39}Ar chronometers. *Geochim. Cosmochim. Acta* **61**, 3477–3501.

Prinzhofer A., Papanastassiou D. A. and Wasserburg G. J. (1992) Samarium–neodymium evolution of meteorites. *Geochim. Cosmochim. Acta* **56**, 797–815.

Qin L., Dauphas N., Wadhwa M., Masarik J. and Janney P. E. (2008) Rapid accretion and differentiation of iron meteorite parent bodies inferred from ^{182}Hf–^{182}W chronometry and thermal modeling. *Earth Planet. Sci. Lett.* **273**, 94–104.

Renne P. R., Swisher C. C., Deino A. L., Karner D. B., Owens T. and Depaolo D. J. (1998) Intercalibration of standards, absolute ages and uncertainties in $^{40}Ar/^{39}$ Ar dating. *Chem. Geol.* **145**, 117–152.

Righter K. and Drake M. J. (1997) A magma ocean on Vesta: core formation and petrogenesis of eucrites and diogenites. *Meteorit. Planet. Sci.* **32**, 929–944.

Sack R. O. and Ghiorso M. S. (1991a) Chromian spinels as petrologic indicators: Thermodynamics and petrological applications. *Am. Mineral.* **76**, 827–847.

Sack R. O. and Ghiorso M. S. (1991b) An internally consistent model for the thermodynamic properties of Fe–Mg–titanomagnetite–aluminate spinels. *Contrib. Mineral. Petrol.* **106**(4), 474–505.

Satterwhite C. and McBride K. (2007). *Antarctic Meteorite Newsl.* **30**, 2.

Sessler R., Hess P. C. and Ruutherford M. J. (1982) Liquidus relations in the forsterite–silica–anorthosite–albite system at 1 atmosphere. *Lunar and Planetary Science XIII*, 710–711.

Shafer J., Neal C. R., Castillo P. (2004) Compositional variability in lavas from the Ontong Java Plateau: results from basalt clasts within the volcaniclastic sequence of Ocean Drilling Program Leg 192 Site 1184. In: Origin and Evolution of the Ontong Java Plateau (eds. Fitton J. G., Mahoney J. J., Wallace P. J. and Saunders A. D.). *Journal of the Geological Society of London Special Publications* vol. 229, pp. 333-351.

Sharp Z. D. (1995) Oxygen isotope geochemistry of the Al_2SiO_5 polymorphs. *Am. J. Sci.* **295**, 1058–1076.

Sharp Z. D. (2007) *Principles of Stable Isotope Geochemistry.* Pearson Prentice Hall, Upper Saddle River, New Jersey.

Sharp Z. D., Atudorei V. and Durakiewicz T. (2001) A rapid method for determination of hydrogen and oxygen isotope ratios from water and solid hydrous substances. *Chem. Geol.* **178**, 197–210.

Shearer C. K. and Papike J. J. (2005) Crustal building processes on the Moon: models for the petrogenesis of the magnesian suite. *Geochim. Cosmochim. Acta* **69**, 3445–3461.

Shearer C. K., Hess P. C., Wieczorek M. A., Pritchard M. E., Parmentier E. M., Borg L. E., Longhi J., Elkins-Tanton L., Neal C. R., Antonenko I., Canup R. M., Halliday A. N., Grove T. L., Hager B. H., Lee D.-C. and Wiechert U. (2006) Thermal and magmatic evolution of the Moon. In *New Views of the Moon* (eds. B. L. Jolliff, M. A. Wieczorek, C. K. Shearer and C. R. Neal). Mineralogical Society of America, Washington, D.C, p. 365–518.

Shearer, C.K., Burger, P.V., and Papike, J.J. (2008) Olivine diogenites and QUE 93148. Remnants of the HED parent body mantle? *Lunar Planet. Sci. XXXIX.* #1835 (abstr.).

Shearer C. K., Burger P. V., Neal C. R., Sharp Z., Borg L. E., Spivak-Birndorf L., Wadhwa M., Papike J. J., Karner J. M., Gaffney A. M., Shafer J., Weiss B. P., Geissman J. and Fernandes V. A. (2008) A unique glimpse into asteroidal melting processes in the early solar system from the Graves Nunatak 06128/06129 achondrites. *Am. Mineral.* **93**, 1937–1940.

Shykolyukov A. and Lugmair G. W. (1993) ^{60}Fe in eucrites. *Earth Planet. Sci. Lett.* **119**, 159–166.

Spivak-Birndorf L., Wadhwa M. and Janney P. (2009) ^{26}Al–^{26}Mg systematics in D'Orbigny and Saraha 99555 angrites: Implications for high-resolution chronology using extinct chronometers. *Geochim. Cosmochim. Acta* **73**, 5202–5211.

Steiger R. H. and Jäger E. (1977) Subcommission on geochronology: convention of the use of decay constants in geo- and cosmochronology. *Earth Planet. Sci. Lett.* **36**, 359–362.

Sunshine J.M., Day J.M.D., Ash R.D., McCoy T.J., Bus S.J., Klima R.L. and Hiroi T. (2009) Searching for the evolved crust of oxidized asteroids. *Lunar Planet. Sci. XL.* #1965 (abstr.).

Swindle T. D., Isachsen C. E., Weirich J. R. and Kring D. A. (2009) ^{40}Ar–^{39}Ar ages of H-chondrite impact melt breccias. *Meteorit. Planet. Sci.* **44**, 747–762.

Takahashi E. (1983) Melting of a Yamato L3 chondrite (Y 74191) up to 30 kbars. *Memoirs Natl. Inst. Polar Res.* **30**, 168–180.

Takeda H., Ishii T., and Otsuki M. (2001) Mineralogy of inclusions in the Campo del Cielo and Mont Dieu irons and segregation of partial melts. *Lunar and Planetary Science XXXII.* Lunar Planetary Institute, Houston. #1183 (abstr.).

Taylor G. J., Keil K., McCoy T., Haack H. and Scott E. R. D. (1993) Asteroid differentiation: pyroclastic volcanism to magma oceans. *Meteoritics* **28**, 34–52.

Teng F. Z., Wadhwa M. and Helz R. T. (2007) Investigation of magnesium isotope fractionation during basalt differentiation. Implications for a chondritic composition of the terrestrial mantle. *Earth Planet. Sci. Lett.* **261**, 84–92.

Thrane K., Bizzaro M. and Baker K. (2006) Extremely brief formation interval for refractory inclusions and uniform distribution of [26]Al in the early Solar System. *Astrophys. J.* **646**, L159–L162.

Treiman A. H., Morris R. V., Kring D. A., Mittlefehldt D. W., and Jones J. H. (2008) Petrography and origin of the unique achondrite GRA 06128 and GRA 06129: preliminary results. *Lunar and Planetary Science XXXIX*. Lunar Planetary Institute, Houston. #2215 (abstr.).

Turner G., Busfield A., Crowther S. A., Harrison M., Mojzsis S. J. and Gilmour J. (2007) Pu, Xe, U, Pb chronology and isotope systematics of ancient zircons from Western Australia. *Earth Planet. Sci. Lett.* **261**, 491–499.

Valley J. W., Kitchen N., Kohn M. J., Niendorf C. R. and Spicuzza M. J. (1995) UWG-2, a garnet standard for oxygen isotope ratios: strategies for high precision and accuracy with laser heating. *Geochim. Cosmochim. Acta* **59**, 5223–5231.

Van der Marel H. W. and Beutelspacher H. (1976) *Atlas of Infrared Spectroscopy of Clay Minerals and their Admixtures*. Elsevier Scientific Publishing, New York, 396p.

Wadhwa M. (2008) Redox conditions on small bodies, the Moon, and Mars. In *Reviews in Mineralogy and Geochemistry* (eds. G. J. MacPherson, D. W. Mittlefehldt and J. H. Jones) vol. 68. Oxygen in the Solar System, pp. 493–510.

Wadhwa, M. and Russell, S. S. (2000) Timescales of accretion and differentiation in the early solar system: The meteoritic evidence. *In Protostars and Planets IV* (eds. Vince Mannings, A. P. Boss and S. S. Russell). University of Arizona Press, Tucson, AZ. p. 995-1018.

Wadhwa M., Shukolykov A., Lugmair G. W. (1998) [53]Mn–[53]Cr systematics in Brachina: a record of one of the earliest phases of igneous activity on an asteroid. *Lunar and Planetary Science XXIX*. Lunar Planetary Institute, Houston. #1480 (abstr.).

Wadhwa M., Srinivasan G. and Carlson R. W. (2006) Time scales of planetesimal differentiation in the early solar system. In *Meteorites and the Early Solar System II* (eds. D. S. Lauretta and H. Y. McSween). University of Arizona Press, Tucson, p. 715–731.

Willmore C. C., Boudreau A. E. and Kruger F. J. (2000) The halogen geochemistry of the Bushveld complex, Republic of South Africa: implications for chalcophile element distribution in the lower and critical zones. *J. Petrol.* **41**, 1517–1539.

Wood B. J. (1991) Oxygen barometry of spinel peridotites. *Rev. Mineral.* **25**, 417–431.

Yapp C. J. and Pedley M. D. (1985) Stable hydrogen isotopes in iron oxides II. D/H variations among natural goethites. *Geochim. Cosmochim. Acta* **49**, 487–495.

Yapp C. J. and Poths H. (1986) Carbon in natural goethites. *Geochim. Cosmochim. Acta* **50**, 1213–1220.

Zeigler R. A., Jolliff B., Korotev R .K., Rumble D., Carpenter P. K., and Wang A. (2008) Petrology, geochemistry, and likely provenance of unique achondrite Graves Nunataks 06128. *Lunar and Planetary Science XXXIX*. Lunar Planetary Institute, Houston. #2456 (abstr.) (CD-ROM).

Zipfel J., Shukolyukov A. and Lugmair G. W. (1996) Manganese–chromium systematics in the Acapulco meteorite. *Meteorit. Planet. Sci.* **31**, A160.

Associate editor: Alexander N. Krot